# Stellar Halos

Modelling Formation in the L-Galaxies 2020 Semi-Analytic Model

**Geoff Murphy**

**Supervisors:** Dr Robert Yates, Dr Daniel Cunnama, & Dr Shazrene Mohamed

A thesis presented for the degree of Masters in Astronomy


Department of Astronomy
University of Cape Town
South Africa
2020

# Contents

I, Geoff Grant Murphy, know the meaning of plagiarism and declare that all of the work in the thesis, save for that which is properly acknowledged, is my own.

Signed by candidate

# Chapter 1

# Abstract

A study was carried out to determine how well the L-Galaxies 2020 semi-analytic model simulates the stellar halos of galaxies and the intracluster stellar (ICS) components of galaxy clusters. Two galaxy disruption models were tested, namely instantaneous disruption and gradual disruption. Furthermore, two stellar halo profiles were applied to the simulation results: a power-law profile with slope $\gamma = -3.5$ and a Navarro-Frenk-White (NFW) profile. In the latter case, the stellar halo stars follow the distribution of the galaxy's dark matter. It was found that a combination of an NFW profile and gradual disruption provided the best results across the widest range of literature data, namely measurements of stellar halo mass, total stellar mass, stellar mass fractions, and stellar halo iron abundances. Gradual disruption of satellite galaxies also resulted in the central galaxies having more massive stellar halos in comparison to instantaneous disruption. Additional stellar halo formation mechanisms, such as in-situ star formation, were not needed, as the stellar halo masses seen in observations can be obtained in L-Galaxies by considering only tidal disruption of infalling satellite galaxies. The number of high mass accretions into the halos of Milky Way-mass galaxies in the gradual disruption model agreed well with simulation literature. It was found that while central galaxies can induce many disruptions of satellite galaxies (over a thousand in some cases), the majority of the Milky Way-sized stellar halos in L-Galaxies are formed by the disruption of one to fourteen satellite galaxies, in good agreement with simulation literature. A population of galaxies with unexpectedly low stellar halo iron abundances was found. These were determined to be a result of disruptions of high mass, low metallicity satellite galaxies. Furthermore, rather than iron or oxygen, carbon was found to be the dominant element produced by stellar halo stars for the majority of redshifts in most high mass central and satellite galaxies, due mainly to asymptotic giant branch stars. The relative contribution of stellar halo stars was found to be minor, however, with circumgalactic medium enrichment from halo stars in comparison to outflows from galactic stars being on average $\lesssim 1\%$. For clusters with virial masses exceeding $1.6 \times 10^{14} M_{\odot}$, the brightest central galaxy and ICS (BCG+ICS) stars contained 42.44% of the total cluster stellar iron content, while the fraction $\frac{M_{ICS}}{M_{BCG}+M_{ICS}}$ was found to be 82.50%, both results being in good agreement with observation.

# Chapter 2

# Introduction

Numerous observational studies have been conducted on halo stars in Milky Way-scale systems, and the intracluster medium in cluster scale systems, particularly in recent years due to increasingly sensitive equipment as well as more refined observation and reduction techniques. Observational results have shown that the stellar halo is a non-negligible component of galaxies and clusters, for example Sivanandam et al. (2009) and Sand et al. (2011). Stellar halos, as with most galactic components, have long formation timescales, and are furthermore extremely dim and diffuse. Simulations are, therefore, a good companion to observation, as both the formation and present day properties of the stellar halo can be modelled.

The stellar halo refers to the diffuse stellar component surrounding single galaxies, groups or clusters. These stars lie outside the bulge and disk, and can extend far from the galaxy's centre, up to hundreds of kpc. Intracluster light (ICL) refers to the observable light which permeates the space between galaxies in clusters, i.e., the light not arising from the brightest central galaxy or the cluster galaxies. The source of the ICL is the intracluster stellar component (ICS). Again, this refers to the diffuse stellar component around galaxies, but if a particular galaxy is in a cluster, its stellar halo forms part of the larger ICS. The term ICS refers to stellar halos on large, cluster scales, so the terms stellar halo and ICS will be used interchangeably throughout this thesis.

There have been numerous observational studies of the Milky Way's stellar halo, for example Xue et al. (2015), Zuo et al. (2017), Deason, Belokurov, and Sanders (2019), Conroy et al. (2019), and Ishigaki (2020). Among other things, stellar halos provide a means to infer the formation history of galaxies. In a more recent study, Lancaster et al. (2019) provide evidence of a poorly mixed stellar halo component named the "Gaia Sausage". Observations show that high metallicity stars with extremely radial orbits lie in the inner regions of the halo, mixed with isotropic, low metallicity populations. This Gaia Sausage constitutes around 50% of the inner stellar halo. This suggests that at some point in its history the Milky Way underwent a merger with a massive satellite galaxy. While mergers are to be expected, the fact that observing stellar halos can provide insight into possibly individual merger events emphasises the value of this particular area of study.

This is not limited to the Milky Way, however. Given our observational position, observing our own stellar halo is particularly challenging. As such, studying nearby galaxies is another alternative. The fact that stellar halos are sparsely populated despite extending over hundreds of kiloparsecs from galactic centres makes observation extremely difficult. Improved observation methods have begun to mitigate the

difficulty in observing the extremely dim and diffuse stellar halos of distant galaxies. Examples of such studies include Merritt et al. (2016), Monachesi et al. (2016b), and Harmsen et al. (2017).

Furthermore, there have been a considerable number of studies into the ICS components of massive galaxy clusters. In addition to providing insight into the formation history of these massive systems, it is also expected that the baryon content of clusters are representative of the baryon content of the Universe as a whole (Gonzalez, Zaritsky, and Zabludoff, 2007), so it is important that even the most difficult to observe components of said clusters are accurately measured. Further examples of cluster halo studies include Sand et al. (2011), Coccato et al. (2011), Montes and Trujillo (2019), and Cañas et al. (2020).

As the importance of studying stellar halos has become more apparent, simulations of its formation have become more frequent. Monachesi et al. (2016a), for example, simulate the stellar halo metallicity profiles of Milky Way-mass galaxies in Auriga, which is a magneto-hydrodynamical (MHD) model. A similar study is done in Monachesi et al. (2019), but with a focus on stellar halo formation in Milky Way-mass galaxies.

### Observations

Accurately measuring the stellar halo of galaxies is important both for accurate mass estimates, as well as understanding the evolutionary history of these galaxies. Montes (2019) provides a detailed review of available observational literature on the ICL, including a brief discussion on history, as well a description of current results and challenges.

Sivanandam et al. (2009) investigate the contribution of the ICS to intracluster medium (ICM) enrichment in comparison to galactic stars, and argue that the ICS is a non-negligible contributor to the iron (Fe) content of the ICM. Assumptions that only the cluster galaxies contribute to the ICM Fe content result in a disagreement between observation and what is predicted by a standard initial mass function, supernova type Ia (SNIa) rate, and metal loss efficiency. Analysis was carried out on galaxy clusters which had ICL data available, with further selection criteria applied (for example galaxies which have a clear distinction between the brightest cluster galaxy, BCG, and the ICS). The authors find that the BCG+ICS component contributes on average $31^{+11}_{-9}\%$ of the Fe content of the ICM (assuming a certain SNIa model). Furthermore, the authors determine that the ICS makes up 80% of the BCG+ICS enrichment.

The source of the ICL itself is studied in DeMaio et al. (2015). Knowing the properties of the ICL, for example how it differs in clusters at different redshifts, provides an opportunity to infer the history of the interactions in these clusters. Four possible processes which result in the growth of the ICL are put forward, namely disruption of dwarf galaxies, tidal stripping of L* galaxies, violent relaxation following major mergers, and star formation which occurs in the ICM itself (in-situ star formation). L* galaxies refer to those with stellar masses similar to the Milky Way, and are located at the knee of the redshift 0 stellar mass function (Press and Schechter, 1974).

In three out of the four galaxy clusters studied, DeMaio et al. (2015) find negative metallicity gradients in the ICS, i.e. high metallicity stars nearer to the centre of the cluster and low metallicity stars in the outskirts. These gradients are likely due to

L* galaxies which have been tidally stripped by the galaxy clusters being studied. L* galaxies themselves have radial metallicity gradients. During interactions, stars at larger radii are disrupted first, with the populations at smaller radii being disrupted when the L* galaxy is nearer to the cluster centre, producing a radial metallicity gradient in the ICS.

### Simulations

With the importance of the ICL and stellar halo becoming clearer, a range of modelling techniques are now being applied to its study. Monachesi et al. (2019) study the stellar halos of Milky Way-mass galaxies in Auriga, a magneto-hydrodynamic (MHD) zoom-in simulation. Grand et al. (2017) use halos from the EAGLE dark matter only simulation and subsequently re-simulate these halos in Auriga using MHD. Monachesi et al. (2019) use the galaxies from this work in their own study.

The authors find they were unable to replicate the mass and median metallicity of the Milky Way's stellar halo, and a handful of possible reasons are suggested. The Milky Way could have accreted galaxies that are less massive and less metal rich than the simulations, or the Milky Way has had fewer than average accretions in its lifespan. However, M31 shows better agreement, particularly with the most massive galaxies in the simulation. From this, and further results, the authors infer that 90% of M31's stellar halo mass formed from three or fewer satellites, and that one very massive Fe rich satellite contributed to the general properties of its halo.

Fattahi et al. (2019) use the Auriga model to study Milky Way-like systems. They find highly eccentric stellar halo components in a number of galaxies, similar to the observational results of Lancaster et al. (2019). Their simulation results show these high eccentricity stellar halo components can result from a single dwarf galaxy accretion, supporting the conclusions made in the previously described observational results, that the Milky Way accreted a massive satellite galaxy at some point in its history.

This thesis uses the L-Galaxies 2020 semi-analytic model. Semi-analytic models, in the context of astrophysics, analytically describe the evolution of gas and stars, but are informed by the results of other simulations as well as observations. L-Galaxies, in particular, uses a set of coupled differential equations in its modelling of mass and energy exchange between the baryonic components of galaxies. A hydrodynamic simulation would utilise fluid dynamics equations in its modelling of baryonic components, something which can be very computationally expensive, particularly at high resolutions when using many computational particles. A semi-analytic model would treat the stellar component of a galaxy as a single variable, and analytically determine how much of the stellar mass is disrupted, stripped, etc. Adjustments are then made by studying previous simulations and observation results.

One of the key advantages of semi-analytic models over hydrodynamic or N-body simulations, for example, is the speed with which simulations can be run. Semi-analytic models are significantly faster, allowing different physics to be tested without a great deal of computational time investment. An in-depth study of stellar halo and ICS formation in the L-Galaxies semi-analytic model has not been carried out before. Determining how well this model agrees with results from literature is the main aim of this paper.

Furthermore, given L-Galaxies' ability to simulate such a large number of galaxies, there is the opportunity to study how difficult to measure properties might behave,

for example the mass of the ICS as a function of total cluster mass. Very massive clusters are rare in the Universe, so using a model like L-Galaxies could provide insight into properties across a broader range of masses than what is easily available from an observational standpoint.

The importance of the stellar halo and ICS to enrichment is another key aspect of this thesis. Given the faintness of stellar halos, making measurements of their metal production is especially difficult. With L-Galaxies' ability to track individual elements, this study serves as an opportunity to better understand the enrichment of these difficult to observe populations.

Lastly, there is the chance to study just how often galaxies accrete mass into their stellar halos, as well as the masses involved in these interactions. This should provide a better understanding into how galaxies' interaction histories affect their present day stellar halo properties.

# Chapter 3

# L-Galaxies

## 3.1 Outline

This project uses the latest public version of the semi-analytic galaxy formation model L-Galaxies 2020, described in detail in Henriques et al. (2020b). This project re-runs the L-Galaxies code on the dark matter subhalo merger trees produced by the Millennium-I N-body simulation. L-Galaxies employs its own equations to model the gas, stellar, and black hole components of galaxies. It also includes physical processes such as supernova feedback and radio mode feedback from black holes. This subsection will briefly describe the model properties relevant to this study.

When analysing galaxy clusters, the most massive galaxy is considered the central galaxy. Observations commonly refer to this as the brightest central galaxy, or BCG. In the code itself, these are 'type 0' galaxies, and are described in chapter 1.1 of the L-Galaxies 2020 supplementary material (Henriques et al., 2020a), available alongside the journal article. 'Type 1' galaxies are satellite galaxies, i.e. those which are gravitationally bound to the central galaxy.

The model also defines galaxies which have lost their dark matter halos but have not merged with the central galaxy as 'type 2' galaxies. Galaxies are determined to be members of a cluster or not using a friends-of-friends (FOF) algorithm, and any galaxy which falls within the virial radius of a cluster's central galaxy is considered to be a cluster member.

Radius definitions which will commonly be used are $R_{200}$ and $R_{500}$. $R_{200}$ refers to the radius where the cluster mass density is 200 times the critical density. $M_{200}$ is defined as the mass enclosed within this $R_{200}$ radius. It is the same case for $M_{500}$, where the radius now extends to the region of 500 times the critical density (Zubeldia and Challinor, 2019).

## 3.2 Disruption Models

### 3.2.1 Instantaneous Disruption

By default, L-Galaxies utilises instantaneous disruption. If the dark matter density of the central galaxy at the satellite's radius is greater than the baryonic density of the satellite, disruption occurs. Once disrupted, all stellar mass of the satellite is added to the stellar halo of the central galaxy, and all of the gas mass is added to the hot gas of the central galaxy. Since L-Galaxies does not simulate distributions, the mass of the central galaxy's stellar halo is simply increased. While an approximation

to a mass distribution is present using rings (described later), this is only used for satellite galaxies, and is furthermore not implemented in instantaneous disruption.

### 3.2.2 Gradual Disruption/HT09 Disruption

Gradual disruption was introduced in Henriques and Thomas (2010). The code first finds a disruption radius, which is measured from the centre of the satellite galaxy.

This is given by

$$r_{\rm disrupt} = \frac{1}{\sqrt{2}} \frac{\sigma_{\rm sat}}{\sigma_{\rm halo}} r_{\rm sat}, \tag{3.1}$$

where $\sigma_{\rm sat}$ and $r_{\rm sat}$ are the velocity dispersion and radius of the satellite, respectively, and $\sigma_{\rm halo}$ is the velocity dispersion of the central galaxy. The authors find this by assuming an isothermal sphere approximation for both the central and satellite galaxy, and assuming the satellite galaxy follows a circular orbit.

Any stellar or gas matter *outside* this radius is disrupted. Taking the stellar bulge as an example, stars outside $r_{\rm disrupt}$ are completely removed from the galaxy, and the bulge radius then becomes equal to $r_{\rm disrupt}$.

Using this model, galaxies can be partially disrupted, whereas in instantaneous disruption galaxies are always completely accreted into the central galaxy.

This project makes significant enhancements to the gradual disruption code introduced by Henriques and Thomas (2010), in order to make it compatible with the improvements made in L-Galaxies 2020. Firstly, rings were implemented into the disruption. L-Galaxies 2020 has the capability of dividing galaxies' stellar disk and cold gas components into rings. As opposed to rescaling the masses of these two components by the ratio of $r_{disrupt}$ to their radii, it can be determined whether each individual ring lies within $r_{disrupt}$ or not. As an example, if the galacto-centric radius of a particular ring, say ring $j$, is greater than $r_{disrupt}$, **fractionRings[j]** is set to 1. This implies that the entirety of the mass must be disrupted. If the ring radius is smaller, **fractionRings[j]** is set to 0. Partial disruption within rings was also added. In the case where $r_{disrupt}$ lies between two rings, only a fraction of the mass in that ring is disrupted. This fraction is given by

$$\text{fractionRings[j]} = \frac{\text{RingArea}[j] - \pi(r_{\rm disrupt}^2 - \text{RingRadius}[j-1]^2)}{\text{RingArea}[j]}, \tag{3.2}$$

where the factor of $j$-1 refers to the previous, smaller radius ring. The second term in the numerator of eq. 3.2 finds the area the disruption radius occupies in ring $j$. The full numerator finds the area of ring $j$ which lies outside the disruption radius. The equation as a whole then finds the fraction of mass which should be disrupted (assuming a flat mass density profile across all rings).

For example, if $r_{disrupt}$ occupies the inner 10% of the ring, the outer 90% is disrupted. This process does assume that mass is evenly distributed within each ring, but different rings can have different masses contained within them. This is done for both the stellar disk and the cold gas component. The bulges of galaxies are not divided into rings, so the original method of mass transfer is kept in this case.

In the original code, neither the metals ($Z$) nor the individual elements of the stellar halos are updated after the disruption. Therefore, the element and metals

transfer was added for the case where rings are not used. The rings function, particularly that which handles the mass transfer itself, includes individual element transfer, so adding rings to the HT09 disruption code was sufficient.

## 3.3 Disruption Counts

The base L-Galaxies code has no method of recording the number of disruptions a galaxy undergoes. The code was modified to include such a tracker, named **NumDisr**. It was, however, set to only count stellar mass transfer to stellar halos, so gas mass disruptions were not considered. This was done because it is stellar halos and ICS components which are of interest for this project.

Furthermore, disruptions of the stellar disk and stellar bulge of satellite galaxies are the only contributors to disruption counts. If a portion of the satellite galaxy's stellar component is lost to the central, this event contributes to **NumDisr**. If the entirety of the satellite falls into the central without any components breaking apart, this is considered an infall event, and the disruption counter does not increase.

A satellite can contribute to the mass of the stellar halo of the central in either of these two ways, but only mass transfer from the disk or bulge is considered a disruption event, as this is akin to tidal stripping.

## 3.4 Hot Gas Element Evolution

Chapter 1.13 of the supplementary material (Henriques et al., 2020a) details the galactic chemical enrichment model used in the code, which was introduced in Yates (2013). The model tracks 11 individual elements produced by SNII, SNIa, and AGB stars. In a similar manner to the disruption counter, variables were added to the code which: 1) track the mass of chemical elements ejected by SNII, SNIa, and AGB stars in the stellar halo that is added to the surrounding hot gas, and 2) track the elements the galaxy itself adds to the hot gas (through outflows). Hence, the contribution the stellar halo makes to the hot gas component can be found, as well the individual contributions of the three channels. These can also then be tracked with redshift to study their evolution.

# Chapter 4

# Analysis

Given below are descriptions of how the data produced by L-Galaxies 2020 was analysed to ensure fair comparisons to literature. L-Galaxies contains 512 tree files, each containing Millenium-I dark matter merger trees. L-Galaxies models the baryonic components of galaxies using this dark matter data. Tree files 0-9 were mainly used for galaxy analysis, e.g. Fe abundances and stellar halo ages, as these tree have files have a stellar mass function (SMF) representative of the simulation as a whole. For cluster analysis, tree files 0-9, 20, 23, 109, 140, 162, 200, 311, 336, 388, 436, 448, and 497 were used. These 22 tree files contain many of the central galaxies with the most massive dark matter halos.

The choice of disruption model had a noticeable effect on stellar masses in clusters, but it had no effect on the virial masses. L-Galaxies 2020 produced 226 galaxy clusters with $M_{200} > 10^{14} M_{\odot}$, where 61 of these are found in tree files 0-9. On intermediate mass scales (with stellar halo masses in the range $10^{8.6} - 10^{11} M_{\odot}$ and excluding galaxies with no stellar halo component), ∼24000 individual galaxies were present when using gradual disruption, and ∼6000 galaxies when using instantaneous disruption, suggesting the choice of disruption model can have significant impact on galaxy populations. These numbers include galaxies which are isolated, as well as those in clusters.

## 4.1 Galaxy Analysis

### 4.1.1 Stellar Halo Iron Abundance

L-Galaxies tracks 11 individual elements involved in supernovae, mergers, and other physical processes. These are H, He, C, N, O, Ne, Mg, Si, S, Ca, and Fe. This enables the Fe abundance to be found in

$$[\mathrm{Fe/H}] = \log_{10}(\frac{\mathrm{M_{Fe}}}{\mathrm{M_H}}) - \log_{10}(\frac{\mathrm{M_{Fe,\odot}}}{\mathrm{M_{H,\odot}}}), \tag{4.1}$$

where $M_{Fe}$ and $M_H$ are the masses in Fe and hydrogen (H) produced by the code (Yates, 2013). The term which normalises to the Sun is given by

$$\frac{M_{\mathrm{Fe},\odot}}{M_{\mathrm{H},\odot}} = \frac{u_{\mathrm{Fe}}}{u_{\mathrm{H}}} \times 10^{log_{10}(\epsilon_{\mathrm{Fe},\odot})-12}. \tag{4.2}$$

The atomic weights, $u$, used for Fe and H were 55.85 and 1.008, respectively (Meija et al., 2016). $log_{10}(\epsilon_{Fe,\odot})$ is the abundance of Fe in the sun's photosphere in units of 12+log(Fe/H), where a value of 7.50 was used (Asplund et al., 2009). Using the individual element masses present in stellar halo stars (i.e. $M_H$ and $M_{Fe}$), a plot was made of the Fe abundance as a function of the stellar halo mass. Using the default settings, the variables **FracZSNIItoHot** and **FracZSNIatoHot** in the L-Galaxies input file are both set to 0.3. This refers to the fraction of metals produced by SNII and SNIa in the disk which is put directly into the hot gas component of galaxies without first mixing with the interstellar medium. This produced stellar halo metallicities generally larger than literature values. Increasing these two variables to 0.7 improved agreement considerably, while maintaining agreement with other physical features in the model (which are not looked at in this thesis). The two cases for instantaneous disruption are shown in fig. 4.1, and for gradual disruption in fig. 4.2, along with the observational results of Harmsen et al. (2017), Deason, Belokurov, and Sanders (2019), and Conroy et al. (2019), and the hydrodynamical results of Monachesi et al. (2019). A value of 0.7 was used going forward.

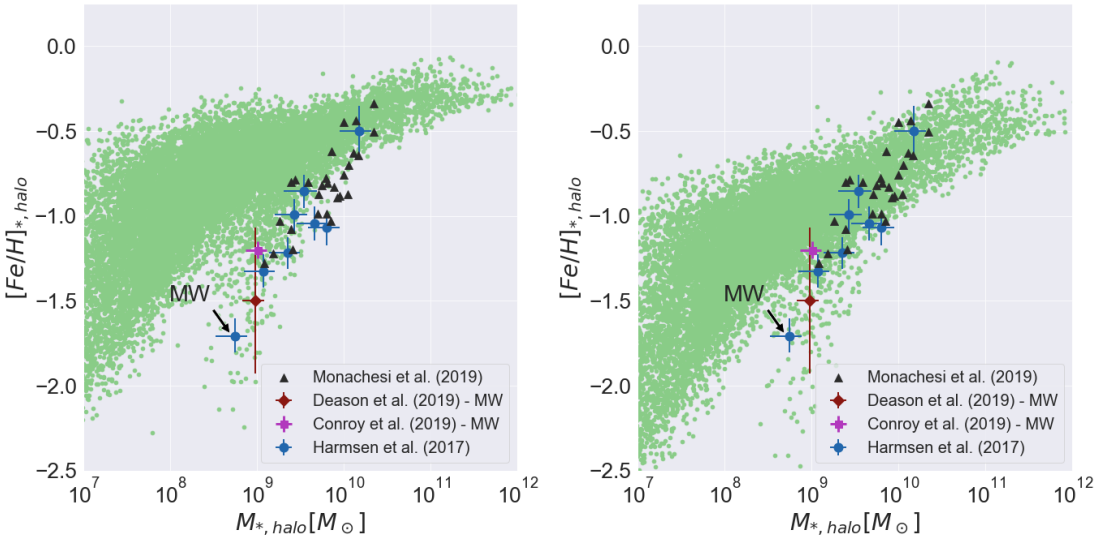


Figure 4.1: Left: The Fe abundance of the stellar halo (for the instantaneous disruption model) when 30% of the metals produced by SNIa and SNII in the disk are deposited into the hot gas component. Right: The Fe abundance when this fraction is increased to 70%. The data point corresponding to the Milky Way in Harmsen et al. (2017) is annotated. Both Deason, Belokurov, and Sanders (2019) and Conroy et al. (2019)'s data points are Milky Way measurements, while the data of Monachesi et al. (2019) is Auriga simulation results.

By increasing the fraction of metals ejected into the hot gas, the metallicity of disk gas, and any stars formed therefrom, is decreased. These disk stars are later transferred to stellar halos through interactions, ultimately decreasing the metallicities of these stellar halos.

The total stellar halo masses measured in Harmsen et al. (2017) are inferred by multiplying the observed stellar halo mass in the range 10-40 kpc by three. As a check, a similar method was carried out with the L-Galaxies results by inferring a Navarro-Frenk-White profile for each galaxy's stellar halo (described in detail in later

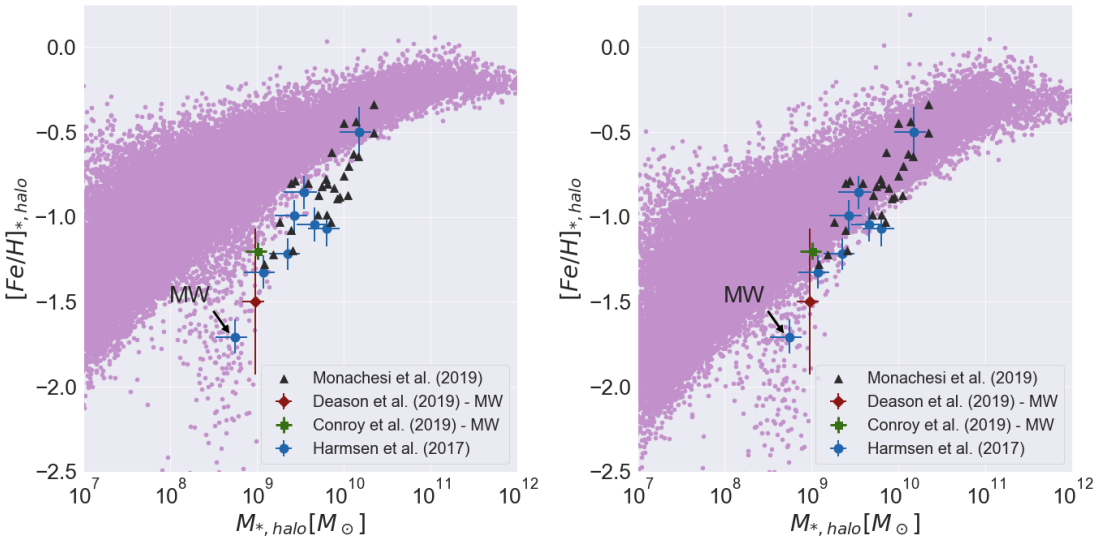


Figure 4.2: The same as fig. 4.1, but for the gradual disruption model.

sections). The stellar halo mass between 10 and 40 kpc was found and multiplied by three, and the results were found to be similar to the total masses produced by L-Galaxies. It was, therefore, found that using the total stellar halo masses produced by L-Galaxies was sufficient, at least on galaxy scales.

### 4.1.2 Ranked Disruptions & Significant Progenitors

By introducing a disruption counter, the number of satellite galaxies disrupted by the galaxy in question can be found. Specifically, each central galaxy has a disruption counter which increases by one each time a disruption event takes place in one of its satellite galaxies. Monachesi et al. (2019), however, consider ranked disruptions, which is dependent on the accreted stellar mass. The authors consider a rank 1 disruption to be the disruption which adds the most mass to the stellar halo overall. A rank 2 disruption adds the second most, etc. The number of significant progenitors is the number of ranked disruptions it takes to form 90% of the total mass of the stellar halo. This analysis was repeated with the L-Galaxies data.

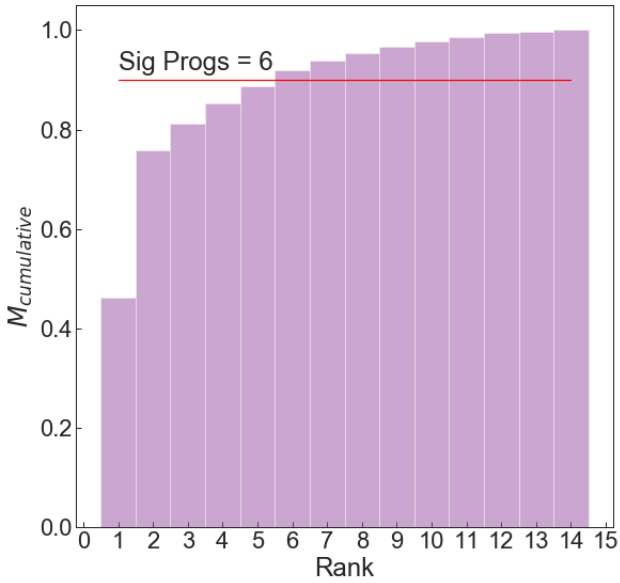


Figure 4.3: An example of how the ranked disruptions of a galaxy might appear. Each bar represents the total stellar mass contributed by a satellite galaxy to the ICS of the central (plotted cumulatively). In this case, there are six significant progenitors.

Fig. 4.3 shows an example of an arbitrary galaxy in which the mass contributions from satellite galaxies are ordered and cumulatively ranked to find the number of significant progenitors. In the instantaneous disruption model, each satellite galaxy is disrupted only once. As such, simply taking the masses added to the ICS and ranking them is sufficient to find the number of significant progenitors. In gradual disruption, galaxies can be disrupted more than once. A counter was added to the data structure which tracks the mass contribution from each satellite galaxy, and is added to in any instance where the satellite contributes mass to the ICS of the central.

In other words, the stellar mass accreted from satellite galaxies is recorded, and the total contribution from each satellite is arranged in rank order. The number of ranked accretion events required to exceed 90% the final ICS mass is defined as the number of significant progenitors. This value was found for all galaxies in tree files 0 to 9 with $1 \times 10^{12} M_{\odot} < M_{200} < 2 \times 10^{12} M_{\odot}$, and the results are compared to the literature in the results section.

## 4.2 Cluster Analysis

Literature values of ICS masses are often dependent on the aperture used. A disagreement between early results and the literature prompted the use of radial distribution profiles for the ICS component of clusters. For example, Morishita et al. (2017) measure the ICS out to 300 kpc, while DeMaio et al. (2020) measure out to 100 kpc. A method was needed to scale the L-Galaxies ICS masses to particular radii, since L-Galaxies does not simulate distributions. Pillepich et al. (2018) find that stellar halos can be described by power-law profiles, while Lin and Mohr (2004) and van der Burg et al. (2015) opt for a Navarro-Frenk-White profile, which is more

commonly used to describe the dark matter distribution of galaxies. Both of these profiles were tested.

L-Galaxies defines type 0 galaxies as those that are at the centre of their friends-of-friends group, with type 1 galaxies being those that are bound to the type 0 galaxy. Additionally, each galaxy has its distance to the central galaxy tracked. Only type 1 galaxies within the virial radius of the central type 0 were considered to be a member of the cluster when calculating total cluster masses. The stellar halo mass of the central and satellite galaxies are summed to give a total ICS mass, and this is then used to set the normalisation of the ICS profile. This process is described in more detail below.

### 4.2.1 Power-Law Profile

For the stellar halo, L-Galaxies calculates a mass, but not a spatial distribution or outer radius. It was assumed that the ICS extends up to the virial radius, $R_{200}$.

Early results using slopes $\gamma \approx -1$ showed good agreement for a number of properties in comparison to literature, but there was no physical motivation for using these values. As such, the shallowest slope ($\gamma = -3.5$) described in Pillepich et al. (2018) was used for the final power-law results. Hence, the power law used was of the form

$$M_{\rm ICS}(r) = \int_{r_{\rm i}}^{r_{\rm f}} A r^{\gamma} dr, \tag{4.3}$$

where $\gamma$ is the slope, $r_i$ and $r_f$ are the integration limits, and $A$ the normalisation. Since the power law tends to infinity at small radii, $r_i$ was set to 1pc. Integrating the above analytically gives

$$M_{\rm ICS}(r) = A(\frac{r_{\rm f}^{\gamma+1} - r_{\rm i}^{\gamma+1}}{\gamma+1}). \tag{4.4}$$

The normalisation, $A$, can be found for each galactic stellar halo or cluster ICS with eq. 4.5,

$$A = \frac{M_{\rm ICS}(\gamma+1)}{r_{\rm f}^{\gamma+1} - r_{\rm i}^{\gamma+1}}, \tag{4.5}$$

where $\gamma = -3.5$, $r_{\rm i} = 1$pc, $r_{\rm f} = R_{200}$ in parsecs, and $M_{\rm ICS}$ is the total ICS mass of the cluster within $R_{200}$. The ICS could then be scaled to a particular radius using eq. 4.3. If the aperture being used was larger than $R_{200}$, the integration was only carried out to $R_{200}$, since it was assumed the ICS does not extend further than this radius.

As stated, the inner integration limit was set to 1 pc. This was chosen so that power law profile could be as closely compared to the NFW profile as possible. The NFW profile has the stellar halo stars follow the distribution of the dark matter (DM) profile. The DM profile extends to 0 pc, but the power law profile diverges at this radius. As such, 1 pc was chosen for both power law and NFW profiles.

While, observationally, stars at this radius would be members of the central galaxy rather than a part of the stellar halo, in the code the difference between using 1 pc and 1000 pc, for example, as an inner radius is negligible. When using an outer scaling radius of 300 kpc for a galaxy with a total stellar halo mass on the order

of $10^{12} M_{\odot}$, the difference between a rescaled mass which uses an inner radius of 1 pc, as opposed to an inner radius of 1000 pc, is of the order $10^{5} M_{\odot}$. This minor mass difference is due to the very large clustocentric radii being used in the rescaling, which in this case are always greater than 100 kpc.

### 4.2.2 Navarro-Frenk-White Profile

The form of the NFW profile is somewhat more complex, but the idea remains the same as the power law profile. The NFW profile, in terms of density, is given by

$$\rho(r) = \frac{\rho_0}{(r/r_s)(1 + r/r_s)^2}. \tag{4.6}$$

The concentration parameter, $c$, is by

$$c = \frac{r_{200}}{r_s}, \tag{4.7}$$

where $r_s$ is the scale radius (Dolag et al., 2004).

The concentration parameter itself (Dolag et al., 2004) is found with

$$c(M, z) = \frac{c_0}{1 + z}(\frac{M}{10^{14} h^{-1} M_{\odot}})^{\alpha}. \tag{4.8}$$

From their simulations, Dolag et al. (2004) found that, in ΛCDM, the concentration normalisation, $c_0$, equals 9.59, and $\alpha$ is -0.102. A value of $h$=0.673 is used. The total ICS mass was used in $M$.

The density was then converted to a mass calculation,

$$M_{ICS} = 4\pi \int_{r_{\rm i}}^{r_{\rm f}} \frac{\rho_0 r^2}{(cr/r_{200})(1 + cr/r_{200})^2} dr \tag{4.9}$$

where only the normalisation, $\rho_0$, remained unknown. Rearranging and inserting the known values into the equation gave

$$\rho_0 = \frac{M_{\rm ICS}^{\rm Total}}{4\pi} \left[ \int_{1{\rm pc}}^{R_{\rm vir}} \frac{r^2}{(cr/r_{200})(1 + cr/r_{200})^2} dr \right]^{-1}. \tag{4.10}$$

In summary, both eq. 4.7 and 4.10 could be solved with values produced by L-Galaxies, where eq. 4.10 was integrated numerically. The ICS mass could then be scaled with eq. 4.9 by replacing $r_{\rm f}$ with the desired radius.

Fig. 4.4 plots these two distributions for the same arbitrary stellar halo mass and radius. Since $dM_{\rm ICS}$ is plotted, integrating over a particular radius range will give the stellar halo mass contained within that range. The power-law profile increases the mass at inner radii by over an order of magnitude, while the NFW profile is significantly flatter. As such, while the same mass is contained in both profiles, only integrating up to $\sim 0.1 R_{\rm vir}$, for example, will result in a greater measured stellar halo mass for the power-law profile.

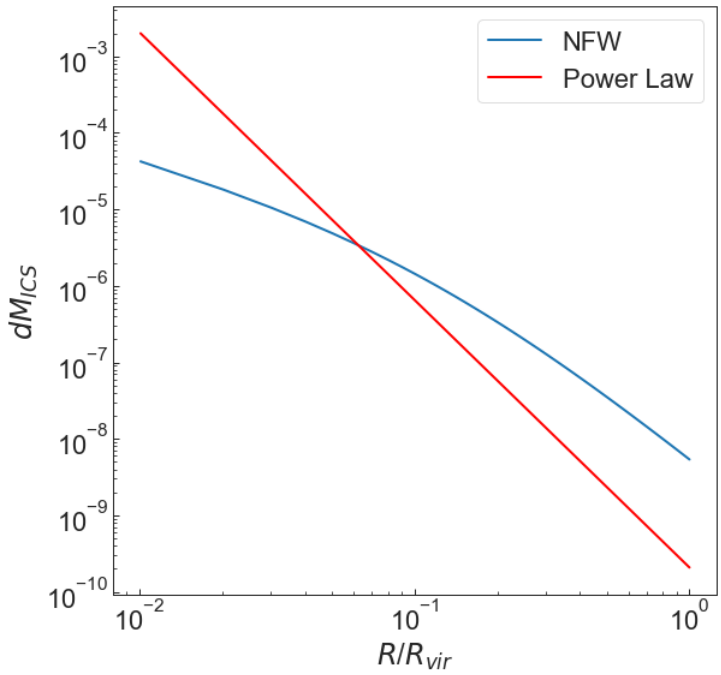


Figure 4.4: A plot of the power-law profile and the NFW profile, using the same arbitrary stellar halo mass and virial radius. The NFW profile is noticeably flatter, spreading the mass more evenly over the same radius compared to the power law profile.

### 4.2.3 Scaling of Literature Data

Morishita et al. (2017) measure ICS data using an aperture of 300 kpc from the cluster centre, while DeMaio et al. (2020) measure to 100 kpc. It was thought that it would be beneficial to scale the former's data to the same aperture, such that both could be compared to one another (specifically in figs. 5.6 and 5.7).

Morishita et al. (2017) provided virial radii, virial masses, and ICS measurements out to 300 kpc. The appropriate profile was used for this scaling procedure, i.e. a power law profile when comparing to the power-law results, and an NFW profile for the NFW results.

In the case of the NFW profile, the concentration parameter in eq. 4.8 could be found from the data provided in Morishita et al. (2017), assuming $c_0 = 9.59$ as before. From this, $r_s$ in eq. 4.7 could be found and substituted into eq. 4.9 to find the total stellar halo mass. The only unknown left in this equation was $\rho_0$, since $r_i$ and $r_f$ were assumed to be 1 pc and 300 kpc, respectively. A search was carried out over a range of possible $\rho_0$ values, and the one which provided a value of $M_{ICS}$ closest to that given in the observational results was taken. Essentially, a full NFW ICS profile was inferred from the data provided, extending to the virial radius. From this, the observational results were rescaled to 100 kpc. The same procedure was carried out for the power-law profile, with the search being done for the normalisation, $A$, in this case.

# Chapter 5

# Results

## 5.1 Cluster Analysis

### 5.1.1 Disruption Models and ICS Profiles

Figs. 5.1 and 5.2 are plots of the ICS mass as a function of $M_{500}$. This is compared to the data of Morishita et al. (2017), which consists of six Hubble Frontier Field galaxy clusters. Morishita et al. (2017) measure the ICS mass by fitting the host galaxy's light profile and the sky background, and infer the ICL contribution through stacking methods. Both the observational data and simulation results are measured out to a clusto-centric radius of 300 kpc. The conversions from $M_{200}$ to $M_{500}$ of the L-Galaxies data were carried out with Colossus (Diemer, 2018), a python package aimed at cosmological analysis.

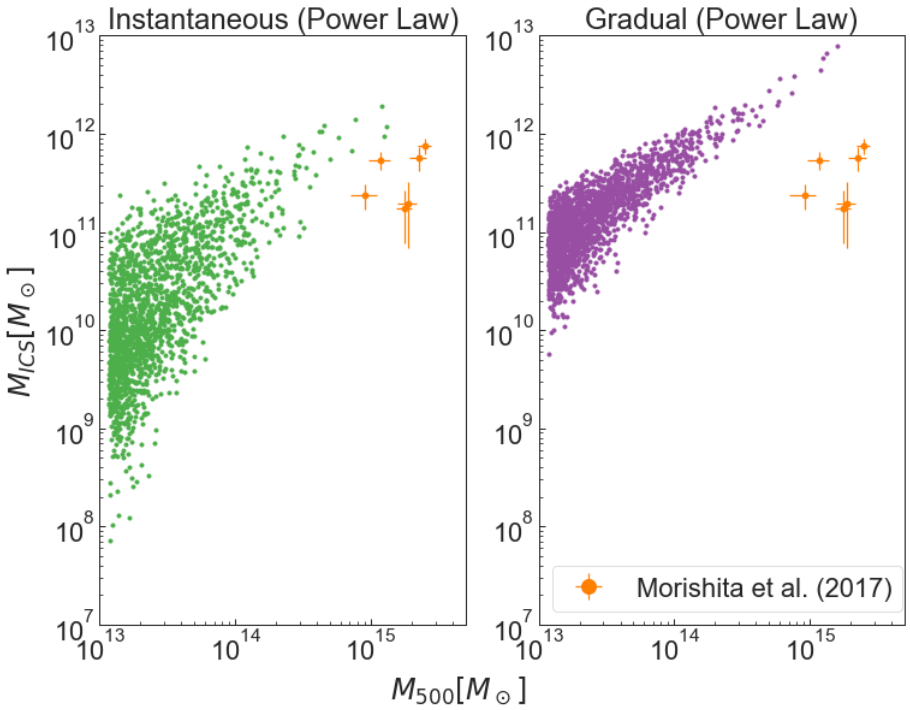


Figure 5.1: The ICS mass out to 300kpc when scaling with a power law profile.

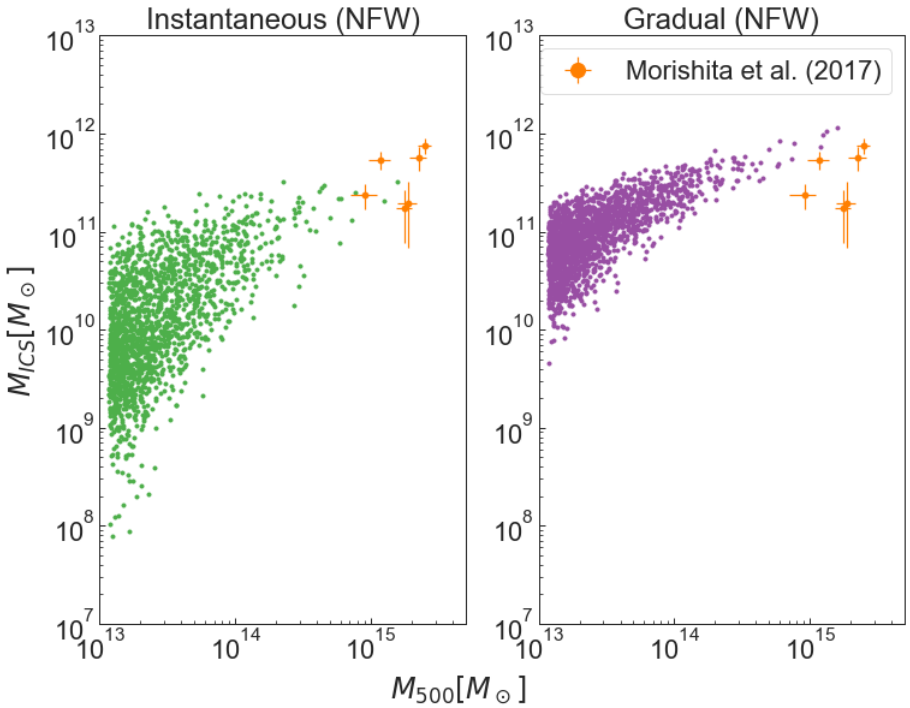


Figure 5.2: The same as fig. 5.1, instead using an NFW profile.

Power-law profiles result in ICS components within 300 kpc which are too massive, likely due to the steepness of this profile. NFW profiles perform better, with Instantaneous+NFW performing the best overall. Gradual+NFW does provide reasonable results, though ICS masses are slightly too high at large $M_{500}$. The $M_{500}$ masses in L-Galaxies, however, only extend up to $10^{15} M_\odot$. This can be seen across all similar results. The fact that the data points are sparse at very high $M_{500}$ masses possibly implies that there are not enough very massive galaxies in the model. This is likely due to the rarity of these massive systems, however. A simulation with a larger box size would have a higher chance of producing these very massive systems. Regardless, in both cases the NFW profile provides the best results.

Figs. 5.3 and 5.4 plot the total cluster stellar mass as a function of $M_{500}$, compared to the observations of Budzynski et al. (2014), which show fits to a set of 20171 groups and clusters. The authors study the relation of stellar mass to $M_{500}$ in SDSS groups and clusters, with the ICL being included in these observations. The authors bin the groups and clusters by total mass, and find the average properties of each bin. Two methods of analysis are used, providing results which either include or exclude the ICL. The aperture used by the authors, and in the stellar halo profiles, was $R_{500}$.

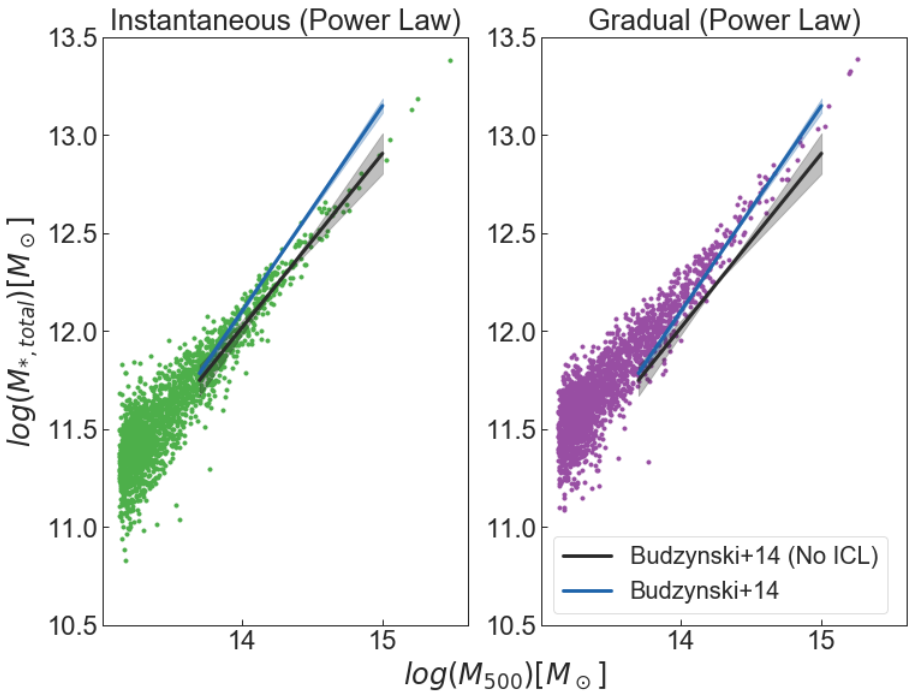


Figure 5.3: The total stellar mass of each cluster. The ICS is scaled with a power law profile using an aperture of $R_{500}$. Budzynski et al. (2014) provide two fits, one including ICL measurements and one excluding.

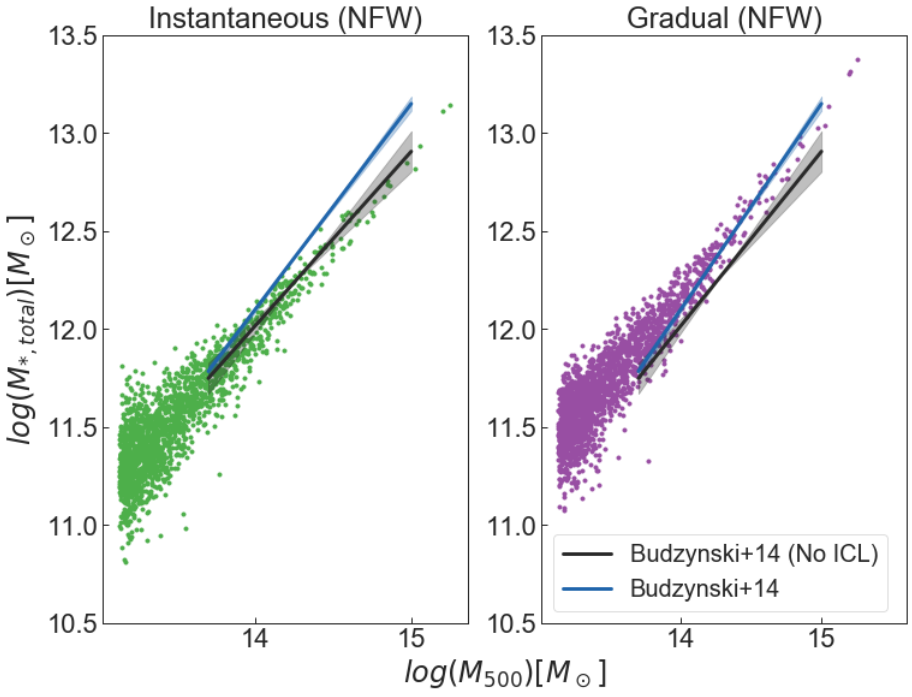


Figure 5.4: The same as fig. 5.3, but for the NFW profile.

The results of figs. 5.3 and 5.4 are very similar, i.e. the difference between the power-law and NFW profile for instantaneous disruption is minor, and the same can be said for gradual disruption. The similarity between the respective disruption models is due to the low mass of the ICS in comparison to the cluster's total stellar mass. Nevertheless, gradual disruption agrees better with the results which include measurements of the ICL.

If a galaxy undergoes instantaneous disruption, it is completely disrupted and the stellar mass is added to the ICS, while the entirety of its cold gas is added to the hot gas component of the central galaxy. No star formation occurs in the ICS in the L-Galaxies 2020 model (although stars which formed in the satellite galaxy before disruption can still produce supernovae). In gradual disruption, a galaxy can be disrupted, but not necessarily completely. The satellite can, therefore, continue to form new stars with the cold gas it still contains. This would ultimately increase the total stellar mass of the cluster in the gradual disruption model, since instantaneous disruption halts any possible star formation in satellite galaxies once they are disrupted.

Here the choice of profile makes little difference, so it is the gradual disruption model which shows the best results.

Fig. 5.5 plots the stellar mass fraction, $f_*$, defined in Budzynski et al. (2014) as the total cluster stellar mass divided by $M_{500}$. Given the relatively minor contribution of the ICS to the total cluster stellar mass, and very high $M_{500}$ masses, the differences between a power law and NFW profile were mostly negligible (similar to figs. 5.3 and 5.4). As such, only the NFW profile results are included, with the purpose of illustrating the differences between instantaneous and gradual disruption.

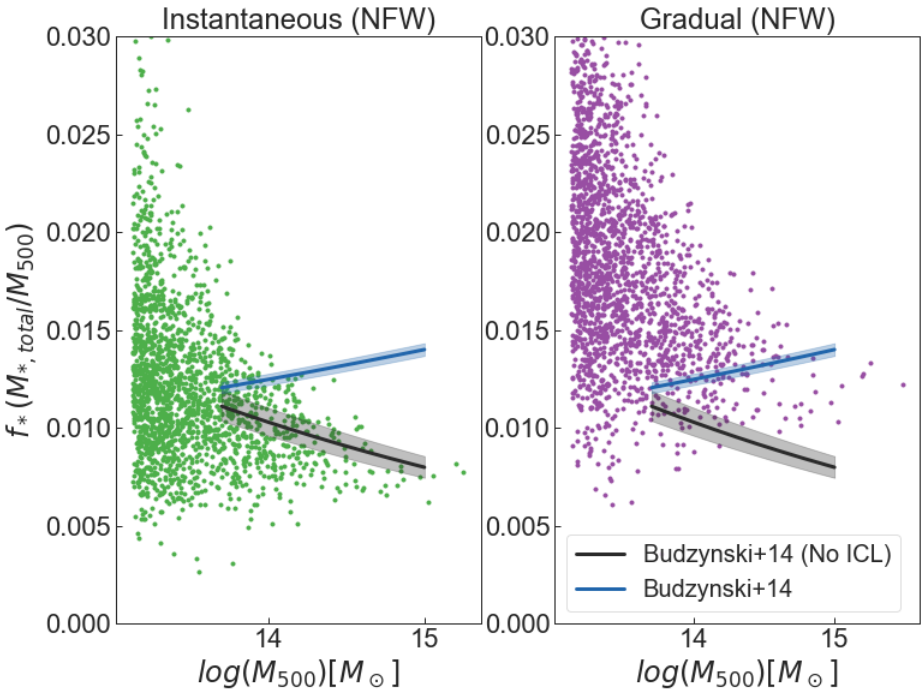


Figure 5.5: The stellar mass fraction, $f_*$ (as defined in Budzynski et al. (2014)), as a function of $M_{500}$. Only the NFW results are given, since the power law results differ negligibly.

As with figs. 5.3 and 5.4, gradual disruption agrees somewhat better with the

results which include the ICS compared to the instantaneous model. This would be due to the increase in total stellar mass (as discussed previously), since the $M_{500}$ masses are similar between disruption models. The L-Galaxies 2020 data shows a wide spread in high $f_*$ values for $M_{500} \lesssim 10^{13.5} M_\odot$, but this region is not covered by the observational results. When comparing to the Budzynski et al. (2014) results, it appears as if the stellar halos of high mass galaxies are not massive enough. Galaxies around $M_{500} \approx 10^{14} M_\odot$ agree well, but this agreement decreases towards $M_{500} = 10^{15} M_\odot$. Increased star formation may be required in L-Galaxies on cluster scales, which would increase $f_*$. Despite the differences in slope, however, the gradual disruption model does produce agreement in the mass range covered by the ICL inclusive literature data.

Figs. 5.6 and 5.7 show the BCG+ICS stellar mass within 100 kpc as a function of $M_{500}$. The ICS data of Morishita et al. (2017) has been scaled from 300 kpc to 100 kpc, since DeMaio et al. (2020) observe the ICL to this radius. Furthermore, DeMaio et al. (2020) analyse clusters in three redshift bins. The intermediate bin contains 23 groups/clusters, and has a mean redshift of 0.4. The particular fit for this bin is chosen, since the data of Morishita et al. (2017) has a mean redshift of 0.42. The appropriate L-Galaxies data corresponding to approximately this redshift was used as well.

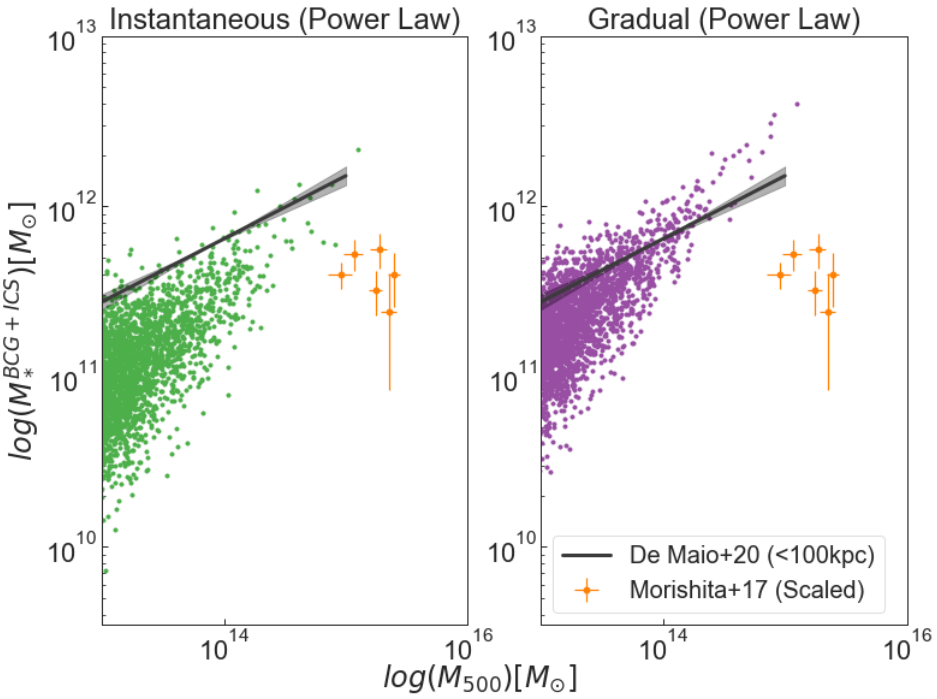


Figure 5.6: The BCG+ICS stellar mass of the clusters, with the ICS scaled to 100 kpc. The Morishita et al. (2017) data was also scaled from 300 kpc to 100 kpc using a power-law profile. This results in noticeably larger error bars due to the log-scaled ordinate. A power-law is used for the rescaling in this case in order to remain consistent with the power-law profile being used for the L-Galaxies ICS mass. As such, fig. 5.7 uses an NFW profile for the rescaling, as the simulation results there use an NFW profile.

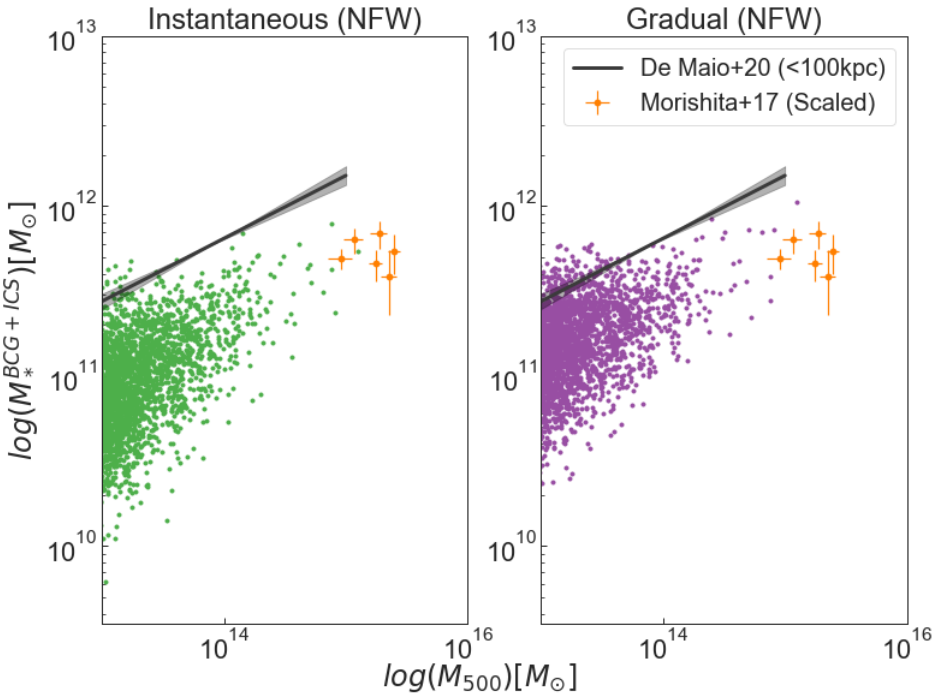


Figure 5.7: The same as fig. 5.6, using an NFW profile for both the L-Galaxies data and the scaling of Morishita et al. (2017)'s data.

The result which performs best is that of Gradual+power law. While the slope is considerably steeper in the L-Galaxies 2020 results, there is good agreement with DeMaio et al. (2020) for $M_{500} < 10^{14} M_\odot$. Other combinations of disruption model and profiles show BCG+ICS masses which are too low in this region. Considering the minimal number of data points in the region of Morishita et al. (2017), agreement with DeMaio et al. (2020) is possibly preferred as this is the region with the highest density of L-Galaxies data points. The two NFW results perform essentially the same as one another, with both showing the correct slope, but little agreement with DeMaio et al. (2020) at high $M_{500}$. Gradual+power law might, therefore, be the best option for high-mass clusters, but not for very high mass clusters ($M_{500} \gtrsim 10^{14} M_\odot$) where instantaneous+power law could be the better option.

Figs. 5.8 and 5.9 plot the ICS to total stellar mass fraction as a function of $M_{500}$. The data of Sand et al. (2011) is included, which is a study on type Ia intracluster supernovae, from which the authors find the stellar halo mass fraction within $R_{200}$. They make corrections for observational biases related to the ease of supernova detection, and their data has a mean redshift of 0.1. As such, the L-Galaxies 2020 data has a redshift of ∼0.1 as well, and an aperture of $R_{200}$ is used for the profiles.

The black box is the authors' main results, assuming stellar halo stars have similar ages to the galactic stars. Assuming the stellar halo stars are exclusively old results in the upper limit above the box. Assumptions on the age have a strong effect on the stellar halo fraction, for example the authors state that younger galaxies have a higher mass to light ratio. Assuming the stellar halo stars are old requires corrections to be made to the observational results, which results in the high upper limit.

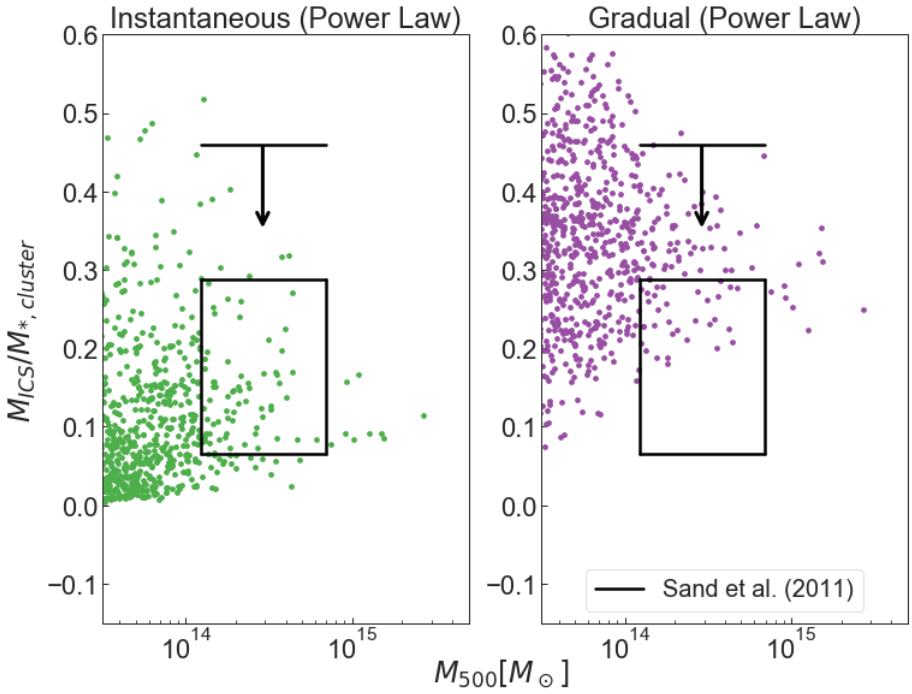


Figure 5.8: A plot of the ICS stellar mass fraction in the power-law model, with the observational data of Sand et al. (2011) included. The authors include an upper limit to the fraction when they assume the stellar halo population is comprised of old stars, as opposed to stars of similar ages to those in the host galaxy.

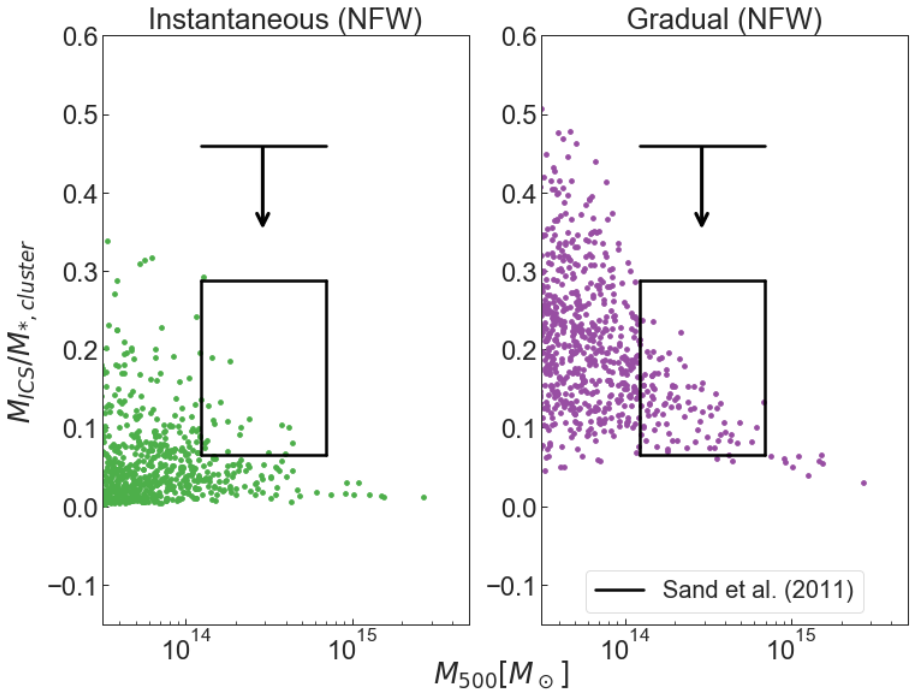


Figure 5.9: The same as fig. 5.8, but with an NFW profile.

Gradual disruption with an NFW profile provides the best results. Instantaneous+NFW has the majority of its data points outside of the Sand et al. (2011) results. While the majority of the data points of the power law results lie below the upper limit, a fair amount also lie outside of the box. Gradual+NFW has essentially all of its points within this box, with only $\sim 2$ points being slightly too low in fraction. Furthermore, all of its data points lie well below the upper limit (in the region covered by the observational results).

### 5.1.2 Cluster Mass Fractions

Sivanandam et al. (2009) provide observational ICS fractions of twelve clusters at $z \lesssim 0.1$. These fractions were looked at in the model as well. Only clusters with virial masses greater than $1.6 \times 10^{14} M_{\odot}$ were considered, as this approximately covers the mass range observed in the paper. This resulted in 149 clusters being used from the L-Galaxies code, sourced from the 22 tree files described at the start of Chapter 4. The aperture used for the NFW profile was $0.6R_{200}$, as was used in the observations. Using the gradual disruption model and an NFW profile, on average and across all clusters, it was found that 42.44% of the total cluster stellar Fe content was contained in the BCG+ICS. This is compared to the value of $31^{+11}_{-9}$% found by Sivanandam et al. (2009). This is a disagreement, within errors, of only 0.44%. Furthermore, the ICS made up 82.50% of the BCG+ICS component in L-Galaxies, where the observations found a mean value of 80% (no uncertainty is given). This level of agreement is good, suggesting that L-Galaxies performs well in terms of BCG and ICS fractions.

Referring to figs. 5.6 and 5.7, the masses of the BCG+ICS components themselves show considerably less agreement when compared to the results of Morishita et al. (2017) and DeMaio et al. (2020). Hence, while stellar masses in these components are too low, the ratio of BCG+ICS to total stellar mass agrees well, suggesting that overall stellar masses in L-Galaxies 2020 possibly need to be increased (at least on cluster scales). However, DeMaio et al. (2020) characterise stellar masses with surface brightness profiles, while Sivanandam et al. (2009) produce stellar mass fractions from Fe abundance measurements. This discrepancy between results could be due to the differing analysis methods.

### 5.1.3 Stellar Halo Mass Function

As one final check of the differences between the two disruption models (on large scales), a plot of the stellar halo mass function was made. This is similar to the regular stellar mass function, but limited to halo stars. There was, unfortunately, no similar observational results found, but this demonstrates somewhat more clearly the effect of the disruption model choice on stellar halo and ICS masses. First, all the masses are log scaled and binned. The counts in each bin are divided by the volume of the simulation and by the bin width being used. The volume is given by $V = \frac{10}{512} \times (\frac{480.279}{h})^3$, where $\frac{10}{512}$ is due to 10 out of 512 tree files being used, and 480.279 is the box side length of the simulation when using cosmology-free units of Mpc/$h$. This box side length is dependent on the dark matter simulation being used, and is set in L-Galaxies' input file. In this case, this particular value is the box side length of the Millenium-I simulation when it is converted from a WMAP-1 cosmology to Planck-1 cosmology. The Planck-I value of $h$=0.673 is also assumed.

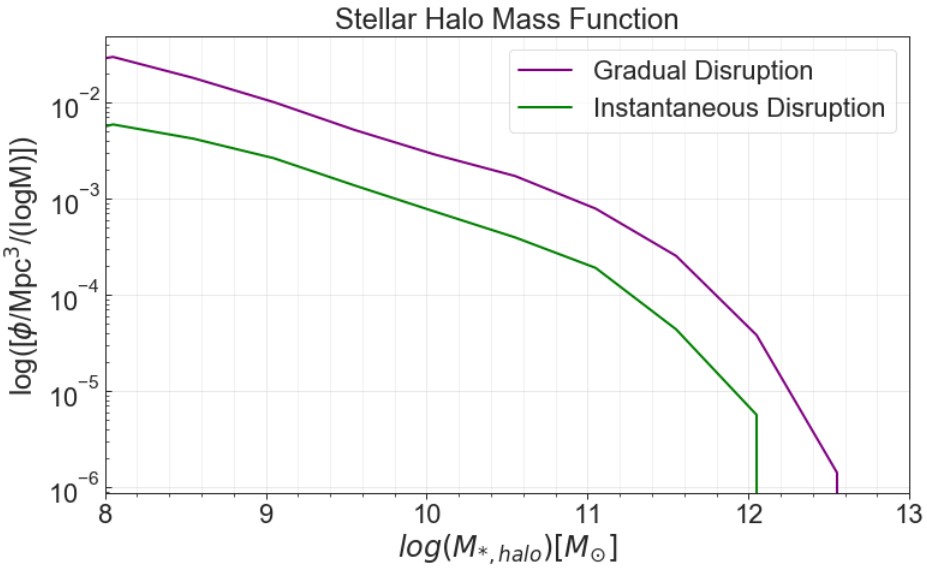


Figure 5.10: The stellar mass function for stellar halo stars for both profiles being used. This is not subject to the low mass cuts made in previous plots, but instead includes all galaxies with non-zero stellar halo masses in tree files 0-9.

This reaffirms what was seen in previous results, that the masses of stellar halos increase when using gradual disruption, and that this is the case for all stellar halo masses above $10^8 M_\odot$. The maximum stellar halo masses present in the model increase by about half an order of magnitude. What is seen more clearly here, however, is that the number of high mass stellar halos increases as well. This could be beneficial when comparing to results similar to DeMaio et al. (2020) (figs. 5.6 and 5.7), in which the BCG+ICS masses are generally larger than that found in the model. Gradual disruption could help in similar cases by increasing stellar halo masses in comparison to instantaneous disruption.

## 5.2 Galaxy Analysis

While the previous section focused on stellar halos on cluster scales, i.e. intracluster stellar components, this section deals with the stellar halos of individual galaxies, be it their metal content, or accretion history. These include galaxies in clusters, as well as isolated galaxies. Galaxies situated in clusters are capable of having their own stellar halos in the L-Galaxies code.

### 5.2.1 Fe Abundances

In order to gauge the metal content of the stellar halo stars, the Fe abundances, [Fe/H], were studied. The results for the instantaneous and gradual disruption models are given in fig. 5.11, which are identical to the right hand plots of 4.1 and 4.2, included here for convenience. Only the data of Monachesi et al. (2019) is simulation results, with the three others being observation.

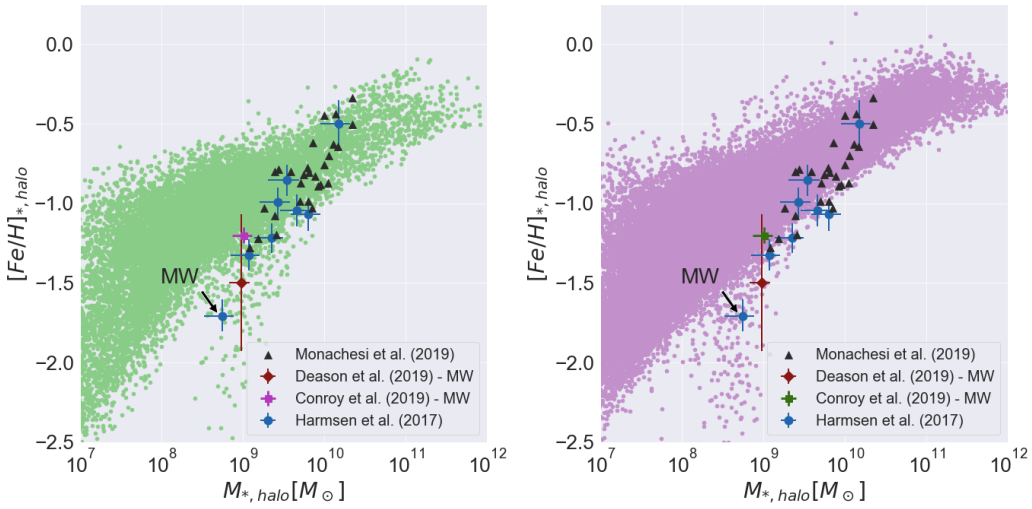


Figure 5.11: The Fe abundances of stellar halo stars in the instantaneous disruption model (left) and the gradual disruption model (right). The L-Galaxies results are plots of Fe abundances using the total Fe and H masses present in the stellar halos of the galaxies.

Both disruption models agree fairly well with the literature data, however the literature shows a significantly steeper slope, suggesting low mass stellar halos are too metal rich in the model while high mass stellar halos are too metal poor. The L-Galaxies 2020 results do manage to reproduce the majority of the data points, however.

Furthermore, while the majority of the literature results lie in the bulk of L-Galaxies data, the Milky Way results (the leftmost point of Harmsen et al. (2017), and the single data points of Deason, Belokurov, and Sanders (2019) and Conroy et al. (2019)) lie towards the low [Fe/H] edge. While the three data points tend to agree with at least one other point within uncertainties, there is a fair amount of difference between stellar halo masses and [Fe/H], likely due to the difficulty associated with making measurements of the Milky Way's stellar halo.

One unexpected feature in the model data was a region of low [Fe/H] values, located at the spur around stellar halo masses of $10^8 - 10^9 M_\odot$. An attempt was made to find the cause of this population.

### 5.2.2 Low Stellar Halo Iron Abundance Galaxies

A number of properties were studied in order to determine what caused this feature. Essentially all data points lie in the range $10^4 < M_{*,halo}/M_\odot \lesssim 3 \times 10^{12}$, although masses below $10^8 M_\odot$ are outside the mass resolution of the simulation. The spur does, however, lie within the mass resolution. The plot of Fe abundances was used again, but with disruption numbers included. This number is a measure of how many times a satellite galaxy has been disrupted by the central galaxy, and it is possible for a single satellite to be disrupted multiple times across timesteps. A 2D histogram was made by binning each data point. The mean number of disruptions of the galaxies in each bin was then found, and plotted as a colour map. The result is shown in fig. 5.12. The same was done for the mass weighted age of each host galaxy

in fig. 5.13. Both plots use the instantaneous disruption model with no stellar halo profile applied.

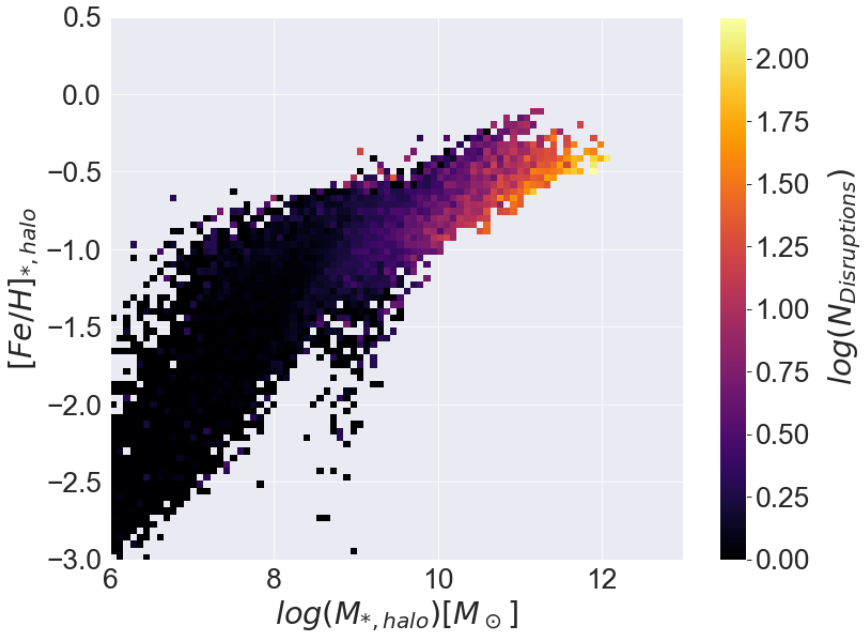


Figure 5.12: A 2D histogram of ICS mass and Fe abundance. Each bin's colour represents the mean number of disruptions of the galaxies in that bin. The disruption numbers are in log scale for clarity.

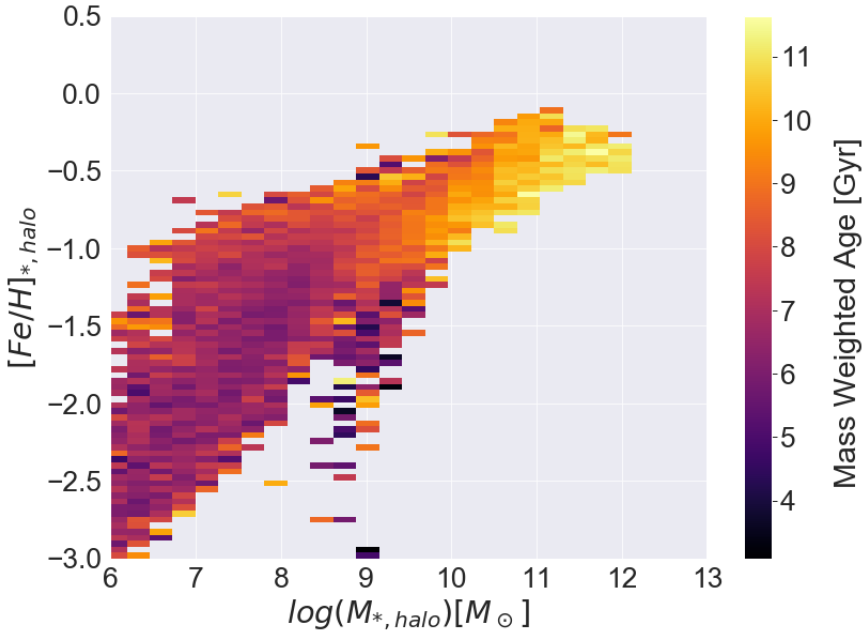


Figure 5.13: A 2D histogram of ICS mass and Fe abundance, coloured by the mean mass-weighted age of the galaxies in each bin.

As expected, the galaxies with the most massive stellar halos have, on average, seen the most disruptions, some over $10^2$ disruptions. While massive galaxies have the majority of their stellar halo mass formed from a handful of disruptions, they still accrete many lower mass satellites into their halos. Compared to smaller galaxies, these massive central galaxies can disrupt satellites more easily.

For clarity, these counts only refer to disruptions which affect stellar masses, so cold or hot gas disruptions were not counted.

Figs. 5.11 - 5.13 include all masses available. Galactic stellar masses (excluding stellar halos) range from $10^7 \lesssim M_{*,gal}/M_\odot \lesssim 10^{12}$, with the stellar halo masses ranging from $0 \lesssim M_{*,halo}/M_\odot \lesssim 10^{12}$. As such, total stellar masses (galactic+halo) range from $10^7 \lesssim M_{*,total}/M_\odot \lesssim 10^{12}$.

The spur at $log(M_{*,halo}) \approx 8.5 M_\odot$ shows a slight decrease in disruption number compared to the galaxies situated in the bulk of the distribution at the same mass. This could suggest that the reduced [Fe/H] is a result of fewer disruptions, but this could also be a statistics issue, given the scarcity of points in this region.

Fig. 5.13 carries out the same analysis, but for the mass-weighted age of each galaxy. The galaxies with the most massive stellar halos are, on average, the oldest. The spur appears to be slightly younger than the population directly above at higher Fe abundances. Again, this could be a statistics issue.

Assuming these properties are physical, since these spur galaxies have similar stellar halo masses as the galaxies above them, but have induced fewer disruptions, the relative masses of the satellites accreted would be higher. In other words, these spur galaxies have disrupted satellites at later times, with the accretions being on the order of $\sim 10^9 M_\odot$. The central galaxies have induced fewer disruptions in comparison to the high Fe abundance galaxies above them in fig. 5.11, and these disruptions are of especially low metallicity satellites.

While it is expected that higher mass satellite galaxies would have higher Fe abundances, this spur region only contains a small number of galaxies, suggesting that galaxies with these properties are rare. The bulk above the spur contains a few thousand galaxies, while the spur itself contains on the order of 100 galaxies, suggesting these galaxies are exceptions to the expected behaviour.

A property which did show considerable differences in the low and high abundances was the stellar halo fraction, shown in fig. 5.14. Two populations were isolated, and their halo fraction distribution was plotted. This was done for the mass-weighted ages of the galaxies as well.

The top-right plot of 5.14 shows that, in comparison to the galactic stellar mass, the low Fe abundance galaxies have a greater stellar halo fraction. This supports the previous suggestion that the spur galaxies have induced fewer, but more massive disruptions.

The bottom plot of 5.14 shows the distribution of the ages of the high and low [Fe/H] populations. Here, the two results are somewhat similar, but the low Fe abundance population contains a number of younger galaxies. This lends some support to the previous statement that the low [Fe/H] spur galaxies are slightly younger, but this shows that a large number of them have similar ages to the high Fe abundance galaxies.

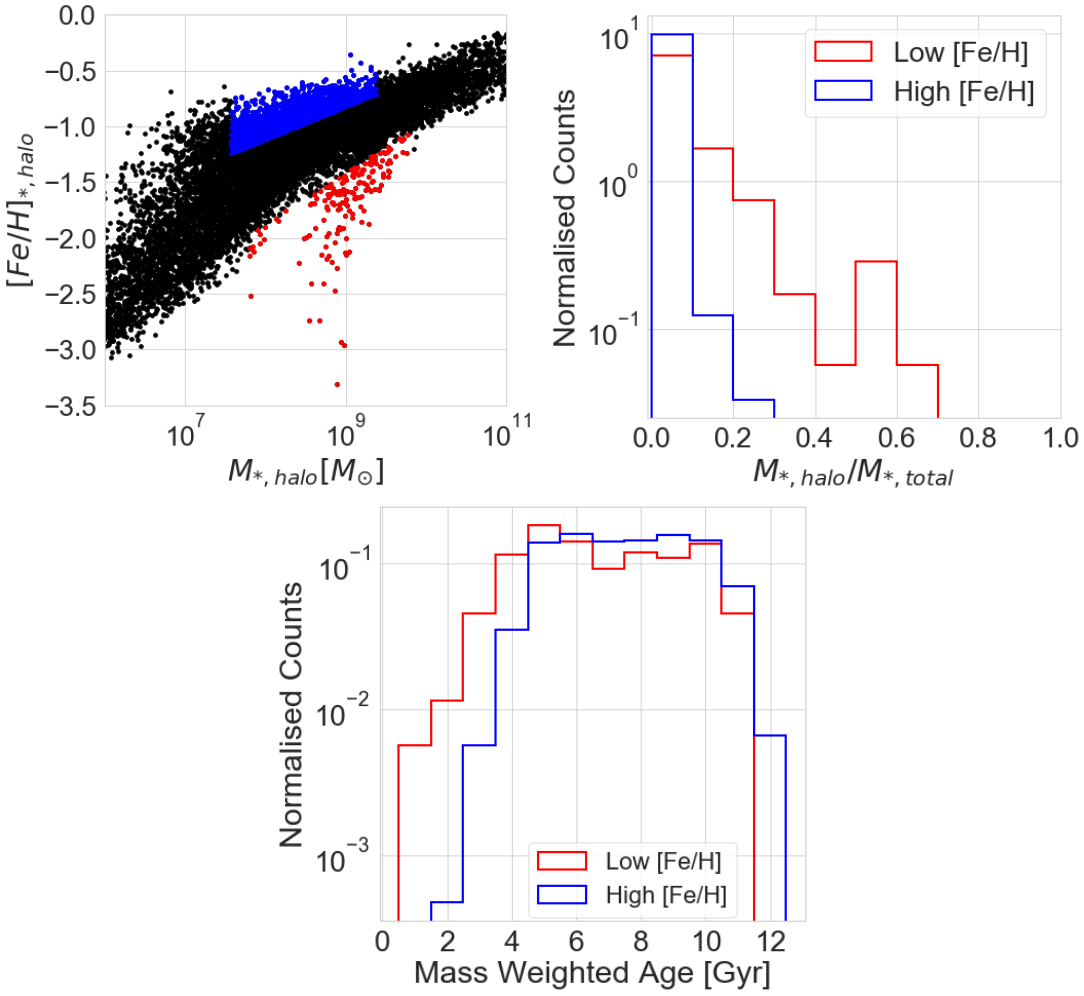


Figure 5.14: Top left: A plot of [Fe/H] with the high and low Fe abundances selected. Top right: A histogram of the stellar halo to total stellar mass fraction of these two selections. Bottom: A histogram of the mass-weighted ages of the two regions.

Additionally, the stellar halo mass and Fe abundance history of these galaxies were studied, with two low [Fe/H] galaxies and two high [Fe/H] galaxy results given in figs. 5.15 and 5.16, respectively. The line colours correspond to the two populations in fig. 5.14. All galaxies are from tree file 0. The main leaf ID of each galaxy is shown at the top of the [Fe/H] evolution plots. Each galaxy belongs to an evolutionary branch which can be followed in the code to track mass and metallicity evolution across redshifts. The galaxy ID of the oldest progenitor of this galaxy is the main leaf ID. All galaxies at all redshifts which are descended from this progenitor have the same main leaf ID. This allows for a single galaxy to be tracked throughout the simulation. Other IDs can change between redshifts, but the main leaf ID remains constant. Figs. 5.15 and 5.16 show the mass and Fe abundance evolution of four central galaxies in the code.

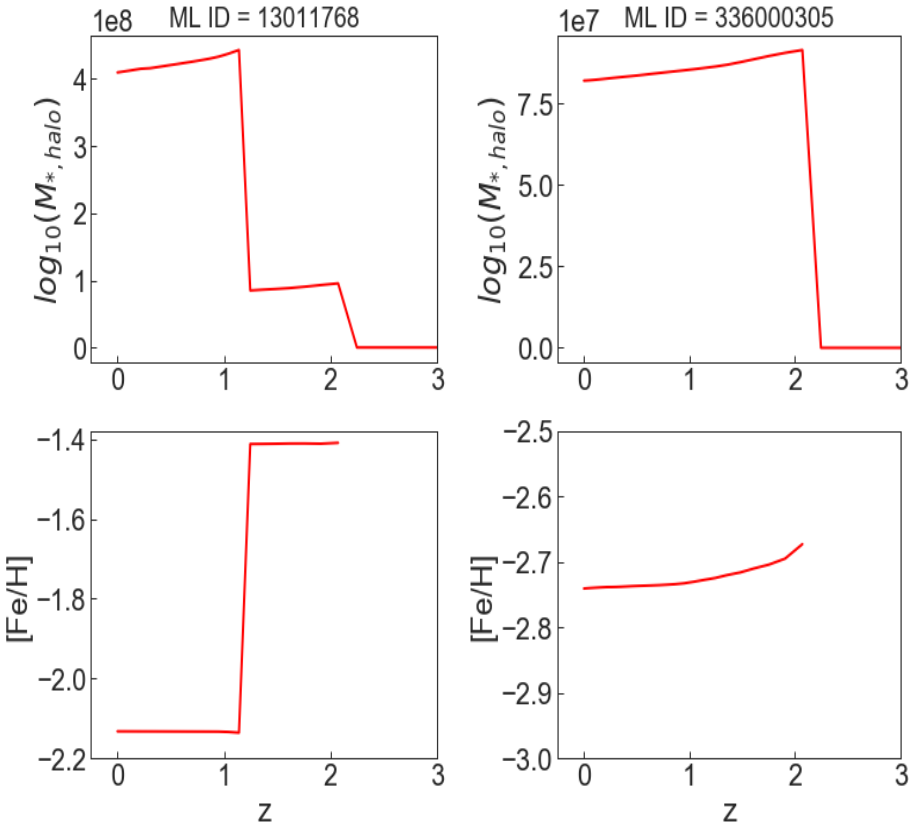


Figure 5.15: The ICS mass (top) and [Fe/H] (bottom) evolution for two low Fe abundance galaxies (the pair of plots on the left corresponding to one galaxy, and the pair on the right to another). Note the order of magnitude at the top left of the stellar halo mass plots.

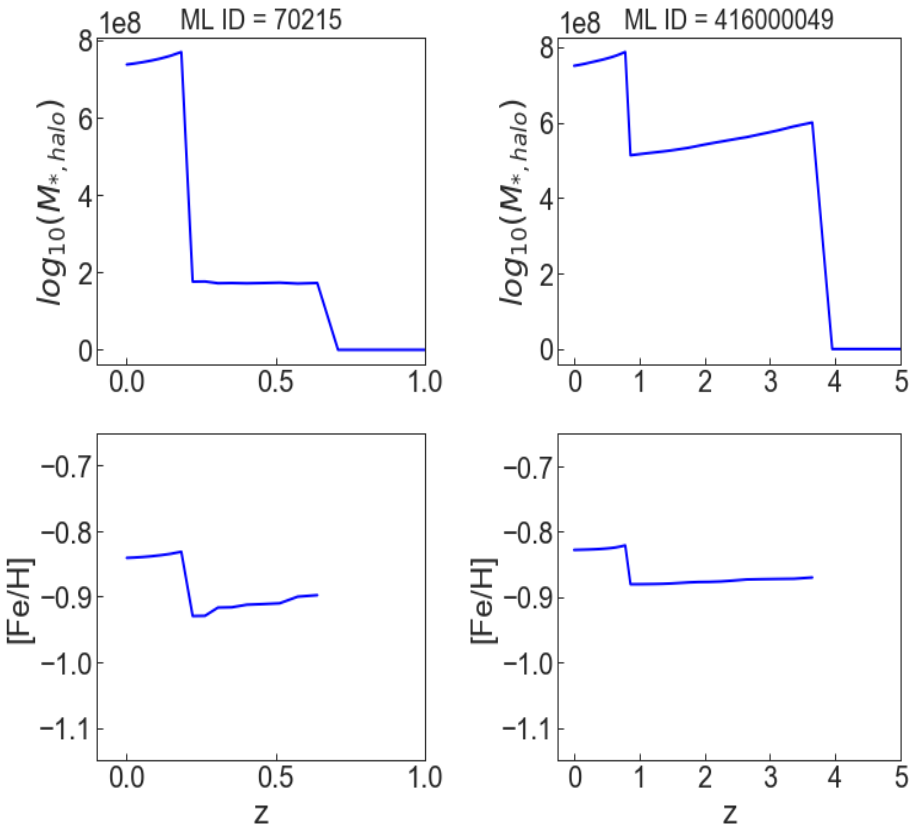


Figure 5.16: The ICS mass and [Fe/H] evolution for two high Fe abundance galaxies.

The evolution plots in figs. 5.15 and 5.16 suggest that the low Fe abundances in some stellar halos are due to accretions of low metallicity galaxies. For all four galaxies shown, a total stellar mass of around $10^7 - 10^8 M_\odot$ is accreted. The main difference is the metallicity of the stars accreted. For example, the galaxy with main leaf ID 13011768 accretes $\sim 10^8 M_\odot$ with a metallicity of -1.4. At $z \sim 1.2$ another accretion takes place, reducing the mean metallicity to -2.1. In comparison, the galaxy with main leaf ID 70215 also undergoes two high mass accretions, but the Fe abundances are in the range $-0.8 \lesssim$[Fe/H]$\lesssim -0.95$, significantly higher than the previous galaxy.

There does not appear to be a relation between accreted stellar mass and the resulting Fe abundance of the central's stellar halo. For example, both main leaf ID galaxy 13011768 and 416000049 accrete mass on the order of $10^8 M_\odot$ into the stellar halo, but the mean Fe abundances are $\sim -1.8$ and $\sim -0.85$, respectively. Rather, the mean stellar metallicity of the satellites they accrete appears to be the dominant factor. The low stellar halo Fe abundance galaxies simply accreted massive, low metallicity satellites, and the high Fe abundance galaxies accreted ones which were high mass and high metallicity.

It is unclear, though, why the spur is restricted to the $10^7 - 10^9 M_\odot$ region. It is possible that lower mass galaxies are not massive enough to induce enough disruptions, while more massive galaxies induce too many disruptions. In other words, high mass galaxies do accrete low [Fe/H] populations, but any low Fe abundance features are suppressed by numerous other disruptions. Low mass galaxies might simply be unable to disrupt the low metallicity galaxies in their neighbourhoods,

thereby limiting the very low [Fe/H] population to one clearly defined region on the Fe abundance-stellar halo mass plots.

As a note, there are significant decreases in stellar halo [Fe/H] values which are not due to accretions. This is most clearly seen in the bottom-right plot of fig. 5.15. There is an accretion at $z \sim 2$, but [Fe/H] continues to decrease thereafter. This can be due to a number of reasons, for example supernovae, stellar winds, or infall events in which a satellite's stellar halo is added to the central galaxy's stellar halo (which is not strictly a tidal disruption event).

As a simple example, if we consider two stars with $\frac{Fe}{H}$ fractions (not Fe abundances which require normalisation to the Sun) $\frac{2}{25}$ and $\frac{7}{80}$, the total $\frac{Fe}{H}$ fraction would be $\frac{2+7}{25+80} = 0.086$. If the more massive star goes supernova, all of its stellar mass is transferred to hot gas, resulting in a reduced $\frac{Fe}{H}$ fraction of $\frac{2+0}{25+0} = 0.080$. While this is a contrived example, it shows how supernovae (and similarly stellar winds) can reduce the Fe abundance.

### 5.2.3 Scaling Iron Abundances

The Fe abundances in fig. 5.11 represent the mean abundance within the entire stellar halo in L-Galaxies. Harmsen et al. (2017), however, measure the Fe abundances at 30kpc. Therefore, a simple scaling procedure was carried out to investigate whether further improvements could be made to the comparison between the L-Galaxies and observed Fe abundances.

We follow Monachesi et al. (2019) by assuming a linear stellar halo metallicity profile. While this is a strong approximation and likely overestimates the steepness of the metallicity profile (especially at large radii), the scaling done here is meant to serve as a simple look into whether scaling is possibly a viable method of improving agreement. For a metallicity profile of the form $Z(r) = mr+c$, Monachesi et al. (2019) find a mean slope of approximately $m = -2.4 \times 10^{-3}$dex/kpc for the accreted-only component of their AURIGA stellar halos.

In a similar manner to the rescaling done for the stellar mass in cluster stellar halos, the Fe abundance of each galaxy's stellar halo is rescaled to 30kpc using this linear profile. For the gradual disruption model, the result is given in fig. 5.17.

This rescaling results in a steepening of the Fe abundance slope, which agrees more closely with the slope of the literature data. Overall agreement is reduced, however, but this shows that rescaling to match the observation methods is a viable strategy in attempting to improve the L-Galaxies results. It is likely that a more physically motivated profile could further improve the L-Galaxies Fe abundances, specifically the issue of the abundances being too high. Further increasing **FracZSNIItoHot** and **FracZSNIatoHot** could also improve this issue by lowering the overall [Fe/H] in the model stellar halos, similar to what was described previously in section 4.1.1.

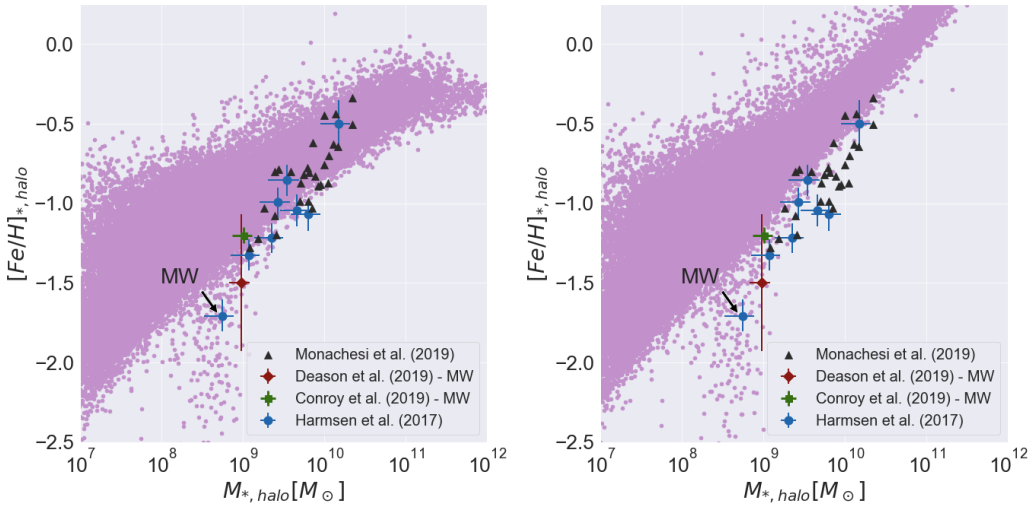


Figure 5.17: Left: The mean Fe abundance of galaxies' entire stellar halos when no profile is applied. Right: The result of a simple rescaling of the Fe abundance in stellar halos using a linear profile. This steepens the slope of the data, but the overall abundances remain too high.

### 5.2.4 Hot Gas Element Abundances

Fig. 5.18 (left) shows the mass in elements released into the ICM by stars in the stellar halo of the most massive galaxy in tree file 0. The right hand plot shows the ICS mass and disruption number history, with the final ICS mass, disruption number, and virial mass printed on the plot.

A characteristic noticed in many massive galaxies which were looked at is that carbon is the most abundant element for the majority of redshifts (excluding hydrogen and helium). It is only at late times that Fe and oxygen become the most abundant. Plotting each channel separately shows that it is asymptotic giant branch, AGB, stars which produce this contribution. Oxygen is the second most abundant element overall, the majority of which is produced by SNII, and Fe is third most, with SNIa being the primary contributor. The individual channels are shown in fig. 5.19.

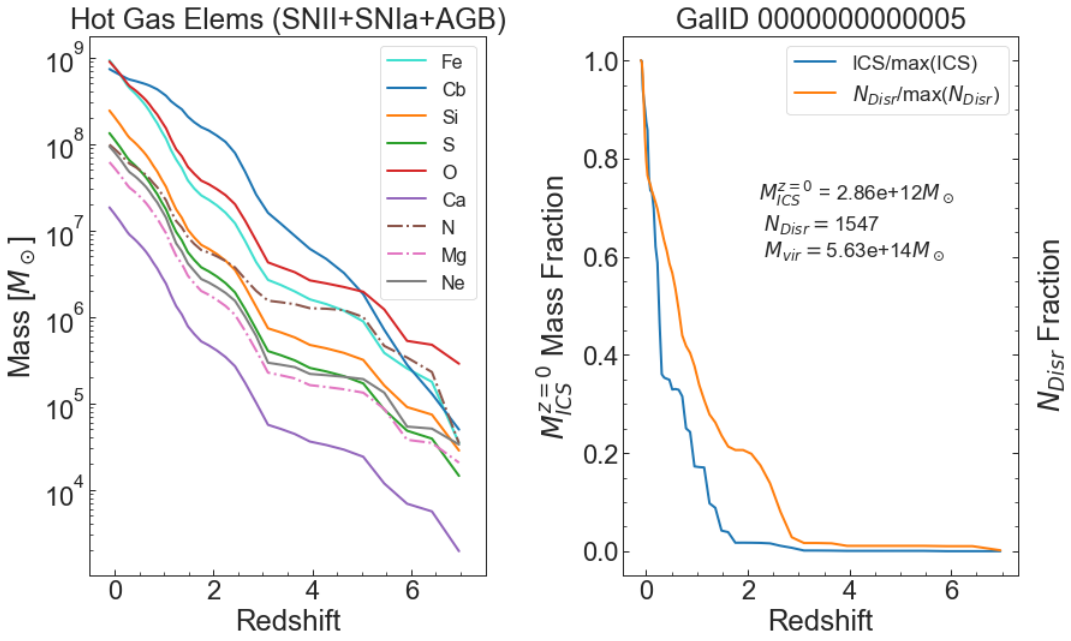


Figure 5.18: Left: The evolution of the ICS contribution to the hot gas component of the most massive galaxy in tree file 0. Right: The ICS mass and disruption number history of this galaxy, with the z=0 values shown.

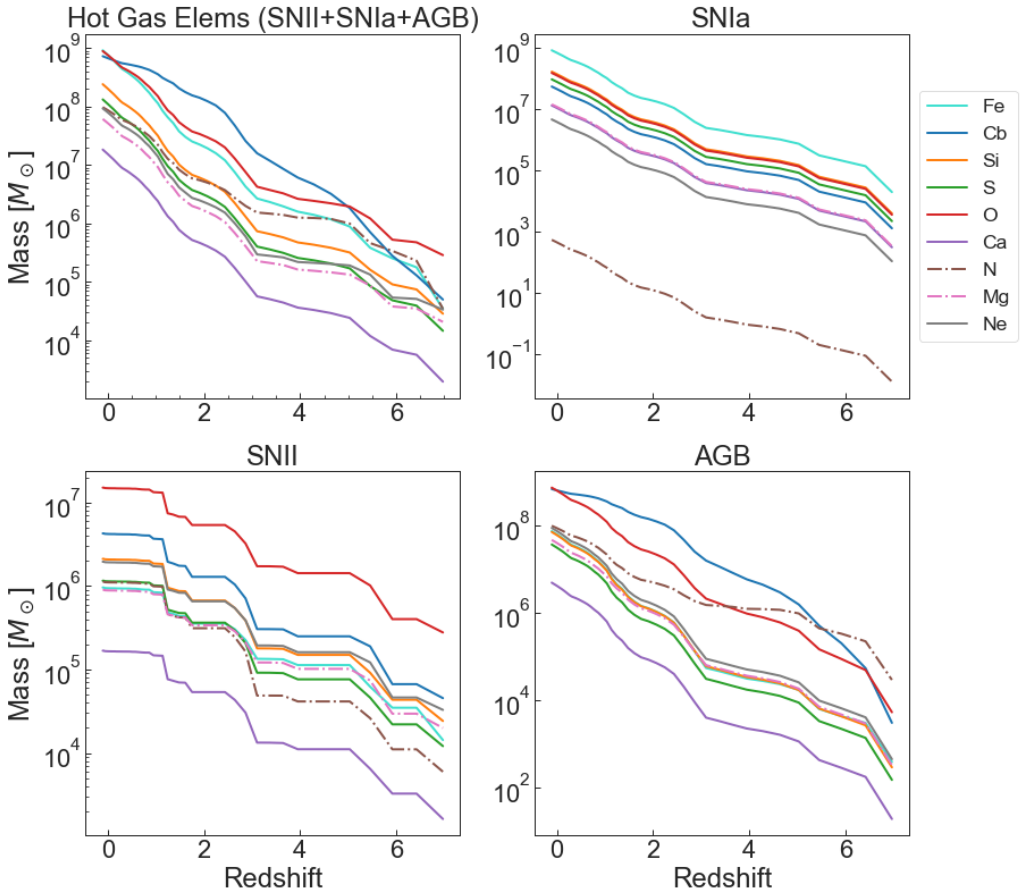


Figure 5.19: The same data as fig. 5.18 (left), split into the individual channels.

This particular galaxy sees the majority of its stellar halo form relatively late,

after $z \approx 2$. This can be said of most of the massive galaxies looked at in the model. Furthermore, there is not one dominant element across all redshifts. For $z > 5$, oxygen is the dominant element. At $0.5 \lesssim z < 5$, carbon is dominant, and Fe is only dominant (along with oxygen) at very late times.

Fig. 5.19 shows each individual contribution from SNII, SNIa, and AGB. The high amount of oxygen at early times is understandably due to SNII, since these are explosions of high mass, short-lived stars. AGB stars are lower mass (El Eid, 2016), and form a great deal of carbon in their evolution. As such, carbon begins to dominate in the hot gas component a significant time after the ICS formation. Lastly, Fe is mainly produced by SNIa, a result of white dwarf explosions in binary star systems (Yoon and Langer, 2004). There is also a greater relative number of AGB stars compared to massive SN progenitors. The SN progenitors could possibly explode before being accreted into the central galaxy's stellar halo, while the longer lifespans of AGB stars would give them the opportunity to be accreted and then to begin enriching the hot gas component.

The key reason as to why carbon is the dominant element across such a long time period is likely the lack of star formation. Since the ICM consists of hot gas, star formation is suppressed. L-Galaxies also does not implement any star formation in stellar halos. This galaxy accretes stellar mass into its stellar halo at around z=7. The massive (but less numerous) stars produce SNII, resulting in most of the abundance of oxygen. Since no massive stars form in the ICS after this, the more numerous intermediate mass stars can steadily produce carbon, resulting in it eventually becoming the most abundant element.

Finally, the most massive AGB stars in the model produce greater amounts of nitrogen and oxygen. Yates et al. (2013) describe that, in L-Galaxies, low metallicity AGB stars with masses greater than $4M_{\odot}$ produce larger masses of nitrogen and oxygen than they do carbon, while AGB stars below this mass produce more carbon. High metallicity AGB stars above $4M_{\odot}$ produce comparable amounts of carbon, nitrogen, and oxygen. Since these higher mass stars evolve more slowly, it is only at later times that the rate of carbon enrichment begins to decrease, and the rate of oxygen enrichment becomes comparable to carbon. This is especially visible from around $z = 1$ in fig. 5.19, where oxygen in both the AGB and top-left plot begins to reach the same level of abundance as carbon.

A few properties regarding relative contributions were checked as well, by finding the mean across a number of systems. The gas mass of the intracluster medium, ICM, is contributed to by both ICS stars and stars in the galaxy itself via outflows. The fraction of the ICS Fe contribution to the total contribution was defined as the ICS deposit fraction, i.e.

$$\text{ICS Deposit Fraction} = \frac{\text{ICM}_{Fe} \text{ From ICS}}{\text{ICM}_{Fe} \text{ From ICS} + \text{ICM}_{Fe} \text{ From Gal}}. \tag{5.1}$$

Across all virial masses, the mean ICS deposit fraction was 0.083% by redshift 0. Fig. 5.20 shows the ICS deposit fraction-$M_{500}$ relation more clearly.

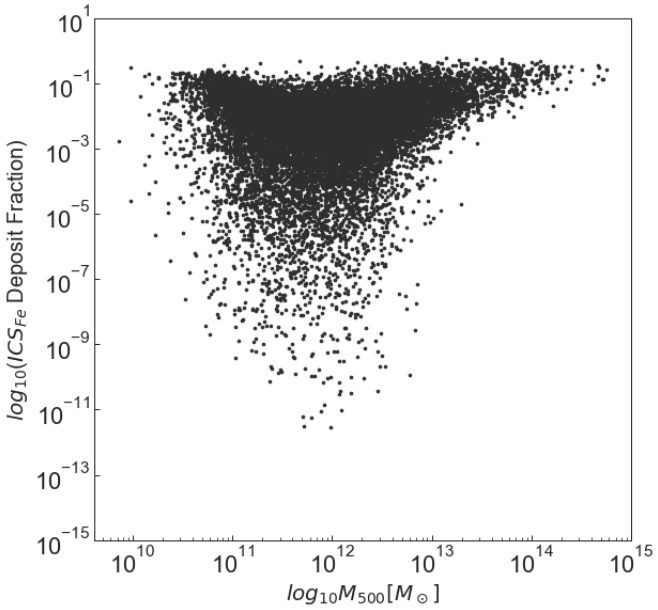


Figure 5.20: A plot of the Fe ICS deposit fraction, i.e. the contribution of the ICS to the Fe content of the ICM, divided by the contribution of the ICS+host galaxy.

Scatter increases towards intermediate masses, and decreases towards the highest masses. It is likely that galaxies with very high $M_{500}$ exist in high mass environments. Any interactions and disruptions would be of high mass satellites, which would in turn produce a massive ICS (for example figs. 5.1 and 5.2). Furthermore, these high mass central galaxies are likely older and contain limited cold gas, which results in limited star formation and consequently limited outflows. Together, this would result in high deposit fractions. Conversely, intermediate mass galaxies do not necessarily form from many interactions. There is less of a guarantee that they would have a massive ICS, and they likely have younger stellar populations with strong outflows, thus resulting in the wide range of deposit fractions. It is difficult to say why the scatter decreases towards the lowest masses, and it cannot immediately be assumed that this behaviour is accurate, since masses this low tend to fall below the simulation's mass resolution. However, it is only the intermediate to high mass systems which are the focus of this project.

### 5.2.5 Disruption Counts

Figs. 5.21 and 5.22 shows the range in disruption number for galaxies with differing $M_{500}$ mass. For both data sets (instantaneous and gradual disruption), the galaxies were split into three $M_{500}$ bins: $10^{9} - 10^{11} M_{\odot}$, $10^{11} - 10^{13} M_{\odot}$, and $10^{13} - 10^{15} M_{\odot}$. Histograms were then made of the disruption numbers in each bin.

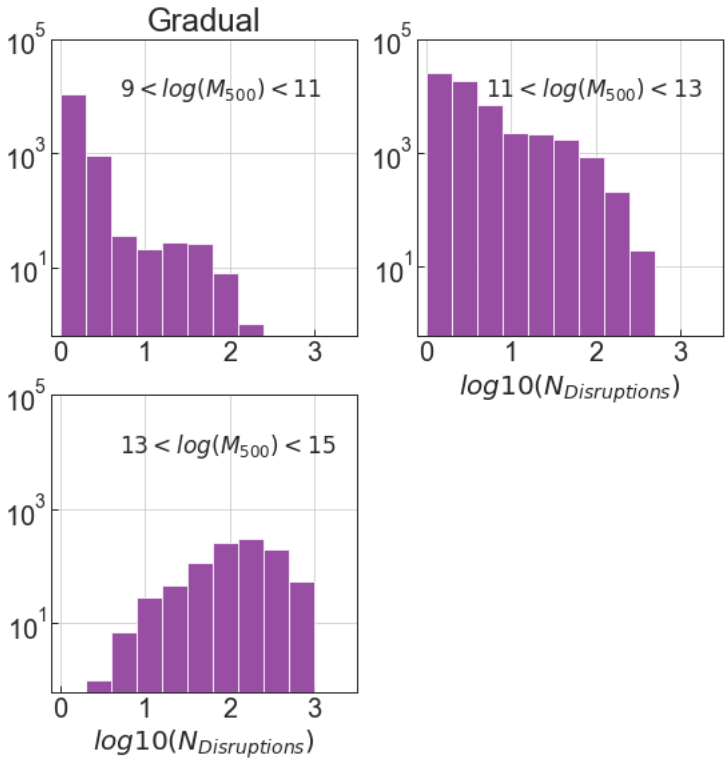


Figure 5.21: The disruption number evolution with $M_{500}$ in the gradual disruption model.

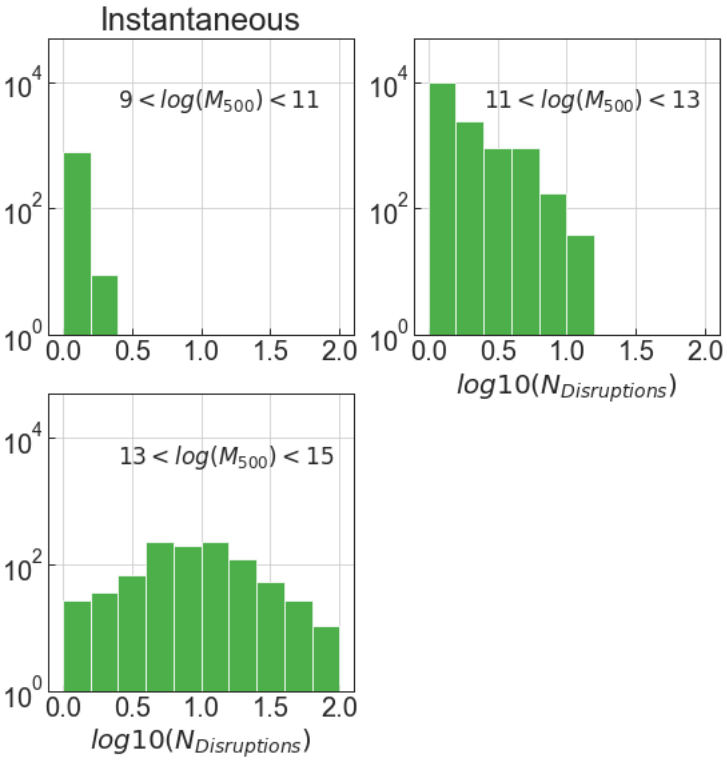


Figure 5.22: The disruption number evolution with $M_{500}$ in the instantaneous disruption model.

For gradual disruption, the data showed that the maximum number of disruptions increases from ∼200 to ∼400, and from ∼400 to ∼2000 between the three bins. Only the highest mass bin shows no bias towards lower disruption numbers, and instead shows a slight peak in the middle of the distribution. This suggests that the most massive systems have not necessarily undergone a large number of disruptions. Furthermore, the lowest mass bin is heavily biased to low disruption numbers, the intermediate mass bin less so, and the highest mass bin shows a peak towards higher $N_{\text{Disruptions}}$, so the mean number of disruptions appears to be dependent on the $M_{500}$ mass.

Instantaneous disruption shows greatly reduced disruption numbers, with the highest being ∼100. The two highest mass bins show similar properties as gradual disruption. The lowest mass bin however only has a maximum of 3 disruptions, with two disruptions being the most frequent, as found from the original data. The main difference between instantaneous and gradual disruption is the maximums, both the maximum disruption number and total counts for each bin. Low mass systems appear to be most affected by the choice of disruption model.

The reduced number of disruptions in low mass systems for instantaneous disruption compared to gradual disruption is understandably due to the different disruption criteria used. However, should a low mass satellite be disrupted in instantaneous disruption, it is completely added to the central galaxy. In gradual disruption, this satellite galaxy can be partially disrupted multiple times, while in instantaneous disruption a galaxy is either disrupted once or not at all. If a satellite is disrupted multiple times in gradual disruption, the disruption counter of the central galaxy is increased each time this disruption occurs.

### 5.2.6 Significant Progenitors

Figs. 5.23 and 5.24 show the number of significant progenitors plotted against the ICS mass of Milky Way-mass galaxies. Monachesi et al. (2019) simulate galaxies in the mass range $1 \times 10^{12} M_{\odot} < M_{200} < 2 \times 10^{12} M_{\odot}$. Using 22 tree files (those named at the beginning of chapter 4), the same mass selection was applied to the L-Galaxies data. Monachesi et al. (2019) only consider the stellar halo mass which arises from accretions, i.e. excluding any in-situ star formation. Since the only manner in which the stellar halo forms and grows in L-Galaxies is through accretions, the halo mass plotted here is simply the total mass produced by the simulation (with no stellar halo profile applied).

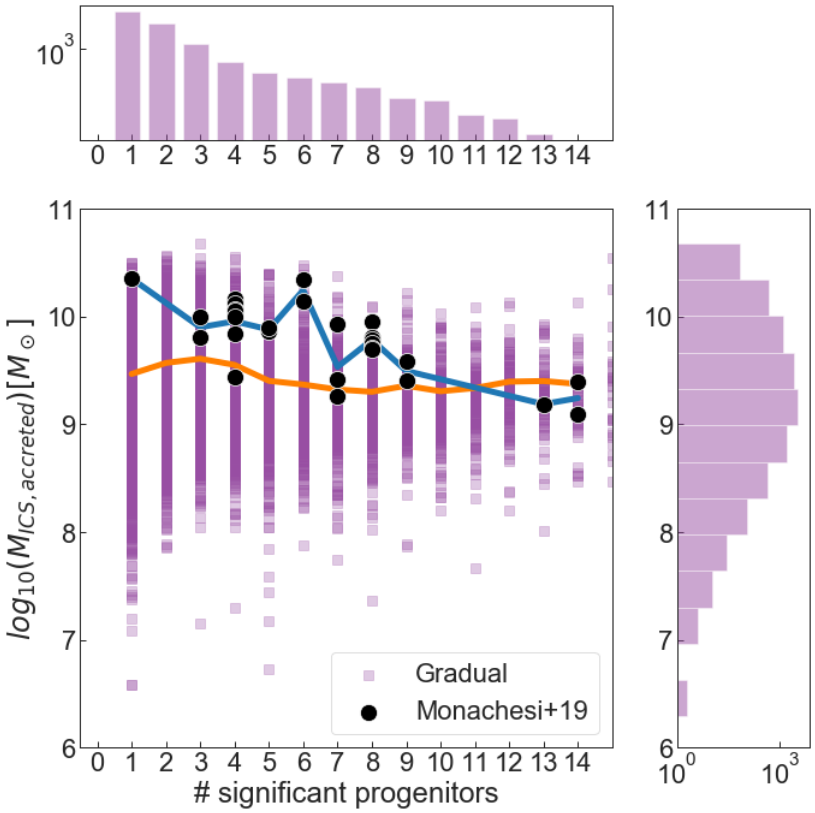


Figure 5.23: The ICS mass-significant progenitor relation found with the gradual disruption code. The blue line shows the mean ICS mass at each significant progenitor for Monachesi et al. (2019), while the orange line does the same for the L-Galaxies results. Distributions are given for the significant progenitor number (above) and ICS mass (right).

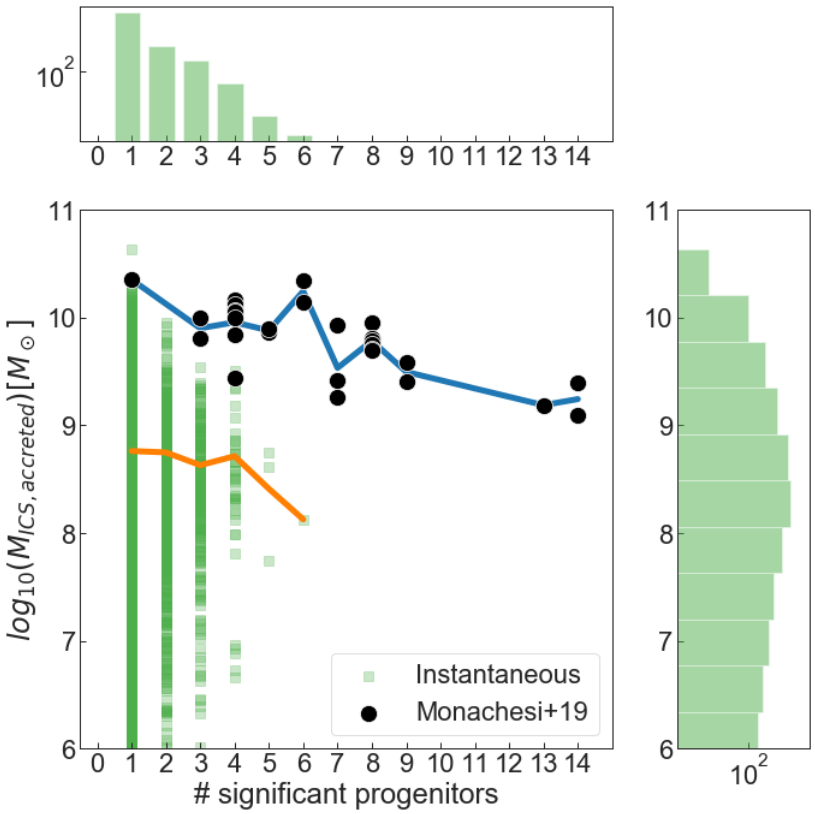


Figure 5.24: The same quantities as fig. 5.23, but for the instantaneous disruption model. Galaxies in this model have significantly fewer significant progenitors, so the plot of the mean ICS mass (orange) only extends to 6 significant progenitors.

The mean ICS mass of the L-Galaxies data (orange line) mostly lies below the mean of Monachesi et al. (2019) for both disruption models. The difference for instantaneous disruption is greater than an order of magnitude, while for gradual disruption it is much less pronounced. Additionally, gradual disruption shows a number of significant progenitors similar to the literature, while instantaneous only shows a maximum of six. The slope of gradual disruption's mean ICS mass is flatter than the Auriga results, but the masses do agree much better than instantaneous disruption.

Gradual disruption, then, shows the best results in terms of significant progenitors. Central galaxies with a low number of significant progenitors have ICS masses which are slightly too low, on average, but towards higher progenitor numbers there is improved agreement.

# Chapter 6

# Conclusions

The stellar halo properties of simulated galaxies in the L-Galaxies 2020 semi-analytic model has been extensively studied in this paper, in particular the specifics of its formation and agreement with literature results.

## 6.1 Disruption Models and Stellar Halo Profiles

Two disruption models were tested: instantaneous disruption and gradual disruption. L-Galaxies does not simulate the distributions of stellar halo stars, so in addition to these two disruption models, two stellar halo profiles were tested. This was a power-law profile with slope $\gamma = -3.5$, and a Navarro-Frenk-White (NFW) profile. Gradual disruption removes the stellar material of satellites over time, while instantaneous disruption immediately deposits the entire satellite galaxy's mass into the central galaxy when the disruption criterion is satisfied.

Overall, gradual disruption produced higher mass stellar halos. Measuring out to smaller radii ($\lesssim 0.1R_{200}$), however, resulted in the power-law profile producing higher masses than the NFW profile, given the power law profile's steeper slope.

On the cluster scale, there is no definitive answer as to which disruption model and stellar halo profile combination matches observational data best. When considering ICS mass as a function of $M_{500}$, Instantaneous+NFW performs best. Gradual disruption with either profile provides the best agreement when looking at total cluster stellar mass with $M_{500}$. Gradual disruption with either profile again performs best for $\frac{M_{*,cluster}}{M_{500}}$ as a function of $M_{500}$.

Furthermore, Instantaneous+power law appears to be the best choice for BCG+ ICS mass as a function of $M_{500}$, and Gradual+NFW performs best when compared to literature results of $\frac{M_{ICS}}{M_{*,cluster}}$ with $M_{500}$. Across all results, though, both disruption models can be made to agree relatively well with literature through a particular profile choice.

On the individual galaxy scale, however, gradual disruption appears to always out-perform instantaneous disruption, specifically in terms of Fe abundances and progenitor histories. Gradual disruption, as stated previously, results in higher stellar halo masses, but also results in a higher number of significant progenitors (the number of galaxies which contribute to 90% of the final stellar halo mass). This provides better agreement with the hydrodynamic simulation results of Monachesi et al. (2019), which shows a maximum of 14 significant progenitors. Gradual disruption covers the full range of the literature data, while instantaneous disruption shows only a maximum of six. Furthermore, the mean stellar halo masses in instantaneous

disruption are significantly lower than the results of Monachesi et al. (2019). The masses in the gradual disruption model agree to a much better degree.

Hence, when looking at galactic scales, gradual disruption is the preferred option. There was no need to apply a radial stellar halo profile when considering the Milky Way-mass observational results used here. For example, Harmsen et al. (2017) measure galaxy stellar halo mass from 10-40 kpc and multiply by 3 to find the total stellar halo mass. Repeating this with the simulation results and halo profiles provided essentially the same results.

The choice is not as easily made on cluster scales, but Gradual+NFW is a good option overall. This combination always agreed at least somewhat well with literature. For example, it out-performed power law results in terms of total cluster stellar mass, despite the ICS components being slightly too massive. It also agreed very well with ICS fractions from literature, specifically $\frac{M_{ICS}}{M_{*,cluster}}$.

Alternatively, while Instantaneous+NFW provided better results for ICS mass, the agreement for total stellar masses was poor. For good BCG+ICS stellar mass agreement, instantaneous disruption would need to be paired with a power-law profile, rather than NFW.

Hence, while Gradual+NFW may perform slightly worse than power law results in some cases, the disagreement with literature is never extreme. This combination can be used for a wide range of results, as opposed to instantaneous disruption, where neither of the two profiles provide good agreement for as wide a range of literature results.

It appears as if the difference in disruption model is most pronounced on galactic scales, compared to cluster scales. Given the long formation time scales and high masses of clusters, how quickly satellites are disrupted, and whether this disruption is complete or partial seems to make minor overall difference. It is likely that the central galaxies are so massive that they suppress any major differences in stellar masses and mass fractions, for example. Of course, there are visible distinctions, but stellar halo profile choice appears to have had a larger effect on the results.

Gradual disruption is more physically motivated, however. It allows satellite galaxies to steadily transfer material to the central galaxy, and only that material which satisfies the disruption criterion. Instantaneous disruption completely and immediately transfers all of the satellite's material, irrespective of whether the satellite barely satisfies the disruption criterion or not. Gradual disruption provides the opportunity for ongoing evolution in the satellite (e.g. star formation and supernovae), either while the galaxy is being disrupted, or after it has been partially disrupted. From a physical perspective, gradual disruption is the most accurate.

As such, gradual disruption in combination with an NFW profile would provide the best results across the widest range of properties while remaining physically consistent. Fine-tuning of this combination could further improve results. For example, either the disruption criterion could be weakened to reduce the slightly too massive stellar halos in clusters, or the stellar halo profile could be flattened further to achieve the same result (when comparing to observation). Regardless, as it is, this model and profile is the preferred choice when comparing to literature.

## 6.2 Stellar Halo Element Properties

Mass fractions in clusters agreed well. In L-Galaxies 2020, the ICS constitutes 82.50% of the BCG+ICS component in clusters with $M_{200} > 1.6 \times 10^{14} M_{\odot}$. Furthermore, the BCG+ICS contained 42.44% of the total cluster stellar Fe content. This was compared to the observational results of Sivanandam et al. (2009), which found fractions of 80% and $31^{+11}_{-9}$%, respectively.

The Fe abundances, [Fe/H], of the stellar halos in L-Galaxies agree well with literature. While the [Fe/H]-$M_{*,halo}$ relation is considerably steeper in the literature, the bulk of the data still agrees with the L-Galaxies results. The literature data is, however, limited to approximately Milky Way masses, while the L-Galaxies data covers a much wider mass range. The fraction of metals put into the hot gas of galaxies had to be increased from 0.3 to 0.7 in order to improve the agreement. Conversely, this decreased the fraction of metals put directly into the star-forming gas inside galaxies from 0.7 to 0.3. Rescaling the L-Galaxies data to match the aperture used in the literature could serve as a means with which to further improve agreement.

In addition, the disruption counts and mass-weighted ages of the galaxies in the Fe abundance plots were studied. Generally, galaxies with higher stellar halo masses had induced more disruptions, and were older. This was not always the case, as was found when studying individual evolution channels, but on average these properties hold.

On an individual basis, the most massive galaxies do not necessarily induce the most disruptions, but the mean number of disruptions was found to be dependent on virial mass. The gradual disruption model also results in higher disruption counts. In this model, the number of disruptions for one galaxy can exceed $10^3$, while for instantaneous disruption the maximum is around $10^2$. This is due to instantaneous disruption completely disrupting the satellite galaxy into the stellar halo of the central galaxy, thereby preventing any future disruptions of that satellite from occurring.

Galaxies with especially low Fe abundances were found in the mass range $10^8 \lesssim M_{*,halo}/M_{\odot} \lesssim 10^{10}$. These galaxies showed higher stellar halo fractions ($\frac{M_{*,halo}}{M_{*,total}}$), but similar ages to the galaxies with higher Fe abundances. Individual evolution plots of these galaxies showed that accretions into the stellar halos on the order of $10^8 M_{\odot}$ occurred, but of especially metal-poor satellite galaxies. These central galaxies possibly have masses which allow them to accrete these low mass satellites, and for these accretions to be clearly reflected in their properties. Lower mass central galaxies are unable to disrupt the satellites, while higher mass central galaxies accrete a greater number of satellites which ultimately suppresses the features of the less numerous low metallicity satellites.

The stellar halo enrichment plots of individual massive galaxies showed that carbon was the most abundant element produced by halo stars for a significant portion of the galaxies' lifespan. Oxygen and Fe were the most abundant only at early and late times. The numerous, but slower evolving, asymptotic giant branch stars were the main source of the carbon, while SNIa and SNII were the main contributors of Fe and oxygen respectively. The hot gas enrichment from stellar halo stars was, however, minor overall. The rate of enrichment by stellar halo stars was $< 1\%$ the rate of enrichment by galactic stars.

By default, L-Galaxies 2020 agrees fairly well with stellar halo results from

observation and from other simulations. The choice of disruption model and stellar halo profile can further improve this agreement considerably. While choosing either instantaneous or gradual disruption, and either a power-law or NFW profile on a case by case may be useful, the choice of one good combination of model and profile can provide good results for a range of cluster properties, in this case gradual disruption and an NFW profile.

L-Galaxies 2020, with an altered gradual disruption model, has also been shown to produce reasonable galactic scale results. While the code's underlying properties, such as mass resolution, limits its agreement with literature in some aspects, there are nevertheless a great deal of results which provide insight into galaxies on this scale.

There is currently a considerable amount of work left to be done on the subject of stellar halos, and L-Galaxies can be a useful tool in this particular field of study, both from an evolution and present day perspective. Its ability to simulate many thousands of galaxies at speed allow for both population, galaxy, and evolutionary studies, without the significant computational time investment required by other simulation models.

# Bibliography


Asplund M. et al. (Sept. 2009). "The Chemical Composition of the Sun". In: *Annual Review of Astron and Astrophys* 47.1, pp. 481–522. DOI: 10.1146/annurev.astro.46.060407.145222. arXiv: 0909.0948 [astro-ph.SR].

Budzynski J. M. et al. (Jan. 2014). "The similarity of the stellar mass fractions of galaxy groups and clusters". In: *Monthly Notices of the Royal Astronomical Society* 437.2, pp. 1362–1377. DOI: 10.1093/mnras/stt1965. arXiv: 1309.1183 [astro-ph.CO].

Cañas R. et al. (Apr. 2020). "From stellar haloes to intracluster light: the physics of the Intra-Halo Stellar Component in cosmological hydrodynamical simulations". In: *Monthly Notices of the Royal Astronomical Society* 494.3, pp. 4314–4333. DOI: 10.1093/mnras/staa1027. arXiv: 1908.02945 [astro-ph.GA].

Coccato L. et al. (Sept. 2011). "Stellar population and the origin of intra-cluster stars around brightest cluster galaxies: the case of NGC 3311". In: *Astronomy and Astrophysics* 533, A138, A138. DOI: 10.1051/0004-6361/201117546. arXiv: 1108.3834 [astro-ph.CO].

Conroy C. et al. (Dec. 2019). "Resolving the Metallicity Distribution of the Stellar Halo with the H3 Survey". In: *Astrophysical Journal* 887.2, 237, p. 237. DOI: 10.3847/1538-4357/ab5710. arXiv: 1909.02007 [astro-ph.GA].

Deason A. J., Belokurov V., and Sanders J. L. (Dec. 2019). "The total stellar halo mass of the Milky Way". In: *Monthly Notices of the Royal Astronomical Society* 490.3, pp. 3426–3439. DOI: 10.1093/mnras/stz2793. arXiv: 1908.02763 [astro-ph.GA].

DeMaio T. et al. (Apr. 2015). "On the origin of the intracluster light in massive galaxy clusters". In: 448.2, pp. 1162–1177. DOI: 10.1093/mnras/stv033. arXiv: 1501.02251 [astro-ph.GA].

DeMaio T. et al. (Jan. 2020). "The growth of brightest cluster galaxies and intracluster light over the past 10 billion years". In: *Monthly Notices of the Royal Astronomical Society* 491.3, pp. 3751–3759. DOI: 10.1093/mnras/stz3236. arXiv: 1911.07911 [astro-ph.GA].

Diemer B. (Dec. 2018). "COLOSSUS: A Python Toolkit for Cosmology, Large-scale Structure, and Dark Matter Halos". In: *Astrophysical Journals* 239.2, 35, p. 35. DOI: 10.3847/1538-4365/aaee8c. arXiv: 1712.04512 [astro-ph.CO].

Dolag K. et al. (Mar. 2004). "Numerical study of halo concentrations in dark-energy cosmologies". In: *Astronomy and Astrophysics* 416, pp. 853–864. DOI: 10.1051/0004-6361:20031757. arXiv: astro-ph/0309771 [astro-ph].

El Eid M. F. (Apr. 2016). "Introduction to Asymptotic Giant Branch Stars". In: *Journal of Physics Conference Series*. Vol. 703. Journal of Physics Conference Series, p. 012005. DOI: 10.1088/1742-6596/703/1/012005.

Fattahi A. et al. (Apr. 2019). "The origin of galactic metal-rich stellar halo components with highly eccentric orbits". In: *Monthly Notices of the Royal Astronomical Society* 484.4, pp. 4471–4483. DOI: 10.1093/mnras/stz159. arXiv: 1810.07779 [astro-ph.GA].

Gonzalez A. H., Zaritsky D., and Zabludoff A. I. (Sept. 2007). "A Census of Baryons in Galaxy Clusters and Groups". In: *Astrophysical Journal* 666.1, pp. 147–155. DOI: 10.1086/519729. arXiv: 0705.1726 [astro-ph].

Grand R. J. J. et al. (May 2017). "The Auriga Project: the properties and formation mechanisms of disc galaxies across cosmic time". In: *Monthly Notices of the Royal Astronomical Society* 467.1, pp. 179–207. DOI: 10.1093/mnras/stx071. arXiv: 1610.01159 [astro-ph.GA].

Harmsen B. et al. (Apr. 2017). "Diverse stellar haloes in nearby Milky Way mass disc galaxies". In: *Monthly Notices of the Royal Astronomical Society* 466.2, pp. 1491–1512. DOI: 10.1093/mnras/stw2992. arXiv: 1611.05448 [astro-ph.GA].

Henriques B. M. B. and Thomas P. A. (Apr. 2010). "Tidal disruption of satellite galaxies in a semi-analytic model of galaxy formation". In: *Monthly Notices of the Royal Astronomical Society* 403.2, pp. 768–779. DOI: 10.1111/j.1365-2966.2009.16151.x. arXiv: 0909.2150 [astro-ph.CO].

Henriques B. M. B. et al. (Feb. 2020a). "L-Galaxies 2020 - Model Description". In: *Monthly Notices of the Royal Astronomical Society* 491.4, pp. 5795–5814. DOI: 10.1093/mnras/stz3233. arXiv: 2003.05944 [astro-ph.GA].

Henriques B. M. B. et al. (Feb. 2020b). "L-GALAXIES 2020: Spatially resolved cold gas phases, star formation, and chemical enrichment in galactic discs". In: *Monthly Notices of the Royal Astronomical Society* 491.4, pp. 5795–5814. DOI: 10.1093/mnras/stz3233. arXiv: 2003.05944 [astro-ph.GA].

Ishigaki M. N. (Jan. 2020). "Chemical abundances of field halo stars - Implications for the building blocks of the Milky Way". In: *IAU Symposium*. Ed. by A. Bragaglia et al. Vol. 351. IAU Symposium, pp. 24–33. DOI: 10.1017/S1743921319007865. arXiv: 1908.09623 [astro-ph.GA].

Lancaster L. et al. (June 2019). "The halo's ancient metal-rich progenitor revealed with BHB stars". In: *Monthly Notices of the Royal Astronomical Society* 486.1, pp. 378–389. DOI: 10.1093/mnras/stz853. arXiv: 1807.04290 [astro-ph.GA].

Lin Y.-T. and Mohr J. J. (Dec. 2004). "K-band Properties of Galaxy Clusters and Groups: Brightest Cluster Galaxies and Intracluster Light". In: *Astrophysical Journal* 617.2, pp. 879–895. DOI: 10.1086/425412. arXiv: astro-ph/0408557 [astro-ph].

Meija J. et al. (Jan. 2016). "Atomic weights of the elements 2013 (IUPAC Technical Report)". In: *Pure and Applied Chemistry* 88, pp. 265–291. DOI: 10.1515/pac-2015-0305.

Merritt A. et al. (Oct. 2016). "The Dragonfly nearby Galaxies Survey. I. Substantial Variation in the Diffuse Stellar Halos around Spiral Galaxies". In: *Astrophysical Journal* 830.2, 62, p. 62. DOI: 10.3847/0004-637X/830/2/62. arXiv: 1606.08847 [astro-ph.GA].

Monachesi A. et al. (June 2016a). "On the stellar halo metallicity profile of Milky Way-like galaxies in the Auriga simulations". In: 459.1, pp. L46–L50. DOI: 10.1093/mnrasl/slw052. arXiv: 1512.03064 [astro-ph.GA].

Monachesi A. et al. (Apr. 2016b). "The GHOSTS survey - II. The diversity of halo colour and metallicity profiles of massive disc galaxies". In: *Monthly Notices of the*

*Royal Astronomical Society* 457.2, pp. 1419–1446. DOI: 10.1093/mnras/stv2987. arXiv: 1507.06657 [astro-ph.GA].

Monachesi A. et al. (May 2019). "The Auriga stellar haloes: connecting stellar population properties with accretion and merging history". In: *Monthly Notices of the Royal Astronomical Society* 485.2, pp. 2589–2616. DOI: 10.1093/mnras/stz538. arXiv: 1804.07798 [astro-ph.GA].

Montes M. (Dec. 2019). "The intracluster light and its role in galaxy evolution in clusters". In: *arXiv e-prints*, arXiv:1912.01616, arXiv:1912.01616. arXiv: 1912.01616 [astro-ph.GA].

Montes M. and Trujillo I. (Jan. 2019). "Intracluster light: a luminous tracer for dark matter in clusters of galaxies". In: *Monthly Notices of the Royal Astronomical Society* 482.2, pp. 2838–2851. DOI: 10.1093/mnras/sty2858. arXiv: 1807.11488 [astro-ph.GA].

Morishita T. et al. (Sept. 2017). "Characterizing Intracluster Light in the Hubble Frontier Fields". In: *Astrophysical Journal* 846.2, 139, p. 139. DOI: 10.3847/1538-4357/aa8403. arXiv: 1610.08503 [astro-ph.GA].

Pillepich A. et al. (Mar. 2018). "First results from the IllustrisTNG simulations: the stellar mass content of groups and clusters of galaxies". In: *Monthly Notices of the Royal Astronomical Society* 475.1, pp. 648–675. DOI: 10.1093/mnras/stx3112. arXiv: 1707.03406 [astro-ph.GA].

Press W. H. and Schechter P. (Feb. 1974). "Formation of Galaxies and Clusters of Galaxies by Self-Similar Gravitational Condensation". In: *Astrophysical Journal* 187, pp. 425–438. DOI: 10.1086/152650.

Sand D. J. et al. (Mar. 2011). "Intracluster Supernovae in the Multi-epoch Nearby Cluster Survey". In: *Astrophysical Journal* 729.2, 142, p. 142. DOI: 10.1088/0004-637X/729/2/142. arXiv: 1011.1310 [astro-ph.CO].

Sivanandam S. et al. (Feb. 2009). "The Enrichment of the Intracluster Medium". In: *Astrophysical Journal* 691.2, pp. 1787–1806. DOI: 10.1088/0004-637X/691/2/1787. arXiv: 0810.1272 [astro-ph].

van der Burg R. F. J. et al. (May 2015). "Evidence for the inside-out growth of the stellar mass distribution in galaxy clusters since z ~1". In: *Astronomy and Astrophysics* 577, A19, A19. DOI: 10.1051/0004-6361/201425460. arXiv: 1412.2137 [astro-ph.CO].

Xue X.-X. et al. (Aug. 2015). "The Radial Profile and Flattening of the Milky Way's Stellar Halo to 80 kpc from the SEGUE K-giant Survey". In: *Astrophysical Journal* 809.2, 144, p. 144. DOI: 10.1088/0004-637X/809/2/144. arXiv: 1506.06144 [astro-ph.GA].

Yates R. M. (May 2013). "The chemical evolution of galaxies in semi-analytic models and observations". URL: http://nbn-resolving.de/urn:nbn:de:bvb:19-171119.

Yates R. M. et al. (Nov. 2013). "Modelling element abundances in semi-analytic models of galaxy formation". In: *Monthly Notices of the Royal Astronomical Society* 435.4, pp. 3500–3520. DOI: 10.1093/mnras/stt1542. arXiv: 1305.7231 [astro-ph.CO].

Yoon S. .-.-C. and Langer N. (May 2004). "Presupernova evolution of accreting white dwarfs with rotation". In: *Astronomy and Astrophysics* 419, pp. 623–644. DOI: 10.1051/0004-6361:20035822. arXiv: astro-ph/0402287 [astro-ph].

Zubeldia Í. and Challinor A. (Oct. 2019). "Cosmological constraints from Planck galaxy clusters with CMB lensing mass bias calibration". In: *Monthly Notices of the Royal Astronomical Society* 489.1, pp. 401–419. DOI: 10.1093/mnras/stz2153. arXiv: 1904.07887 [astro-ph.CO].

Zuo W. et al. (May 2017). "The Stellar Metallicity Distribution of the Galactic Halo Based on SCUSS and SDSS Data". In: *Astrophysical Journal* 841.1, 59, p. 59. DOI: 10.3847/1538-4357/aa70e6.

# Chapter 7

# Acknowledgements

Thank you to my supervisor, Robert Yates, for his constant guidance and support throughout this masters degree, as well as to my co-supervisors, Daniel Cunnama and Shazrene Mohamed for their assistance.